Electron Transport Calculations in Radiotherapy

by

JOHN McLELLAN

A Thesis
Submitted to the Faculty of Graduate Studies
in Partial Fulfillment of the Requirements
for the Degree of

MASTER OF SCIENCE

Department of Physics
University of Manitoba
Winnipeg, Manitoba

(c) copyright John McLellan, August, 1990

National Library of Canada
Canadian Theses Service
Ottawa, Canada
K1A 0N4

Bibliothèque nationale du Canada
Service des thèses canadiennes

The author has granted an irrevocable non-exclusive licence allowing the National Library of Canada to reproduce, loan, distribute or sell copies of his/her thesis by any means and in any form or format, making this thesis available to interested persons.

The author retains ownership of the copyright in his/her thesis. Neither the thesis nor substantial extracts from it may be printed or otherwise reproduced without his/her permission.

L'auteur a accordé une licence irrévocable et non exclusive permettant à la Bibliothèque nationale du Canada de reproduire, prêter, distribuer ou vendre des copies de sa thèse de quelque manière et sous quelque forme que ce soit pour mettre des exemplaires de cette thèse à la disposition des personnes intéressées.

L'auteur conserve la propriété du droit d'auteur qui protège sa thèse. Ni la thèse ni des extraits substantiels de celle-ci ne doivent être imprimés ou autrement reproduits sans son autorisation.

ISBN 0-315-71784-X

Canada

ELECTRON TRANSPORT CALCULATIONS IN RADIOTHERAPY

BY

JOHN McLELLAN

A thesis submitted to the Faculty of Graduate Studies of
the University of Manitoba in partial fulfillment of the requirements
of the degree of

MASTER OF SCIENCE

© 1990

Permission has been granted to the LIBRARY OF THE UNIVERSITY OF MANITOBA to lend or sell copies of this thesis, to the NATIONAL LIBRARY OF CANADA to microfilm this thesis and to lend or sell copies of the film, and UNIVERSITY MICROFILMS to publish an abstract of this thesis.

The author reserves other publication rights, and neither the thesis nor extensive extracts from it may be printed or otherwise reproduced without the author's written permission.

Table of Contents

Acknowledgements..(iii)

List of Figures...(iv)

List of Tables..(vii)

Abstract..(viii)

Chapter 1: Introduction

1.1 Radiation Therapy with Electron Beams...............1

1.2 Linear Angular Scattering Power.....................3

1.3 The Fermi-Eyges Model of Electron Transport.........4

1.4 Dose Computations Using Pencil Beams...............13

1.5 The Purpose of the Present Work....................18

Chapter 2: The Restricted Scattering Model

2.1 The Fermi-Eyges Model: Stochastic Equations Approach..21

2.2 The Restricted Scattering Model: Stochastic Equations Approach................................25

2.3 Comparisons of Mean Square Angle of Travel.........31

2.4 Comparisons of Mean Square Lateral Position........34

2.5 Clinical Beam Profiles.............................38

2.6 Discussion...43

2.7 Conclusion...49

Appendix 2A..50

Appendix 2B..53

Chapter 3: A Numerical Algorithm for Transport Calculations

3.1 Infinitesimal Integral Formula for Small Angles....................................56
3.2 Infinitesimal Integral Formula for Large Angles....................................59
3.3 Numerical Implementation of the Infinitesimal Integral Formula..................................60
3.4 Incorporation of Electron Energy Loss in the Algorithm....................................65
3.5 Requirements for Grid Spacing.....................66
3.6 Calculations in Homogeneous Media: Small Angles....................................69
3.7 Calculations in Homogeneous Media: Large Angles....................................79
3.8 Discussion.................................86
3.9 Conclusions................................88
Appendix 3A..................................89
Appendix 3B..................................91

Chapter 4: Summary and Future Work

4.1 The Restricted Scattering Model..................93
4.2 The Numerical Algorithm..........................95

References.......................................98

Acknowledgements

I would like to acknowledge the financial support of the University of Manitoba and the Manitoba Cancer Treatment and Research Foundation. Ofcourse, the work presented here would not have been possible without the guidance and support of my supervisor, Dr. George Sandison, and acting supervisor, Dr. Walter Huda. Also, I would like to thank Dr. Peter Dunscombe and Dr. J.J. Battista for reading and evaluating the thesis. Most of all, I would like to thank my wife, Yvonne, whose support and encouragement saw me through all those rough times.

List of Figures

Figure 1.1
Coordinate Axis and Angle of Travel....................6

Figure 1.2
The Summation of Pencil Beams to Produce a Broad Beam...15

Figure 1.3
Equivalent Slab Geometry for Calculations in the Presence of an Inhomogeneity..........................17

Figure 2.1
Comparison of Model Predictions of Mean Square Angle of Travel for Constant Scattering Power...............33

Figure 2.2
The Mean Square Angle of Travel versus Depth in Carbon...35

Figure 2.3
The Mean Square Angle of Travel versus Depth in Aluminum..36

Figure 2.4
The Mean Square Angle of Travel versus Depth in Lead...37

Figure 2.5
The Root Mean Square Lateral Position versus Depth in Lung..39

Figure 2.6
The Root Mean Square Lateral Position versus Depth in Bone..40

Figure 2.7
The Root Mean Square Lateral Position versus Depth in Polystyrene...41

Figure 2.8
Broad Beam Profile for 16 MeV Electrons in Lung.......44

Figure 2.9
Broad Beam Profile for 16 MeV Electrons in Bone.......45

Figure 2.10
Broad Beam Profile for 16 MeV Electrons in Polystyrene...46

Figure 3.1
Schematic Diagram for the Propogation of Electrons in the Numerical Algorithm....63

Figure 3.2
Stopping Power for Electrons in Water as a Function of Energy....67

Figure 3.3
Mean Square Angle of Travel versus Depth - Theoretical Calculations and Numerical Algorithm Results....71

Figure 3.4
Mean Square Lateral Position versus Depth - Theoretical Calculations and Numerical Algorithm Results....72

Figure 3.5
Mean Square Angle of Travel versus Depth - Theoretical Calculations and Numerical Algorithm Results....74

Figure 3.6
Mean Square Lateral Position versus Depth - Theoretical Calculations and Numerical Algorithm Results....75

Figure 3.7
Beam Profile at 1.5 cm Depth in Water for an Incident 10 MeV Point Monodirectional Pencil Beam....76

Figure 3.8
Beam Profile at 3.0 cm Depth in Water for an Incident 10 MeV Point Monodirectional Pencil Beam....77

Figure 3.9
Beam Profile at 4.5 cm Depth in Water for an Incident 10 MeV Point Monodirectional Pencil Beam....78

Figure 3.10
Broad Beam Profile at 1.5 cm Depth for a 10 MeV Beam in Water....80

Figure 3.11
Broad Beam Profile at 3.0 cm Depth for a 10 MeV Beam in Water....81

Figure 3.12
Broad Beam Profile at 4.5 cm Depth for a 10 MeV Beam in Water....82

Figure 3.13
Comparison of Pencil Beam Profiles for Small and Large Angle Calculations....84

Figure 3.14
Comparison of Pencil Beam Profiles for Small and Large Angle Calculations..85

List of Tables

Table 1.1
Scattering Constant, k_o, for Several Materials.........5

Table 3.1
Logic Flow for a Numerical Method of Electron Transport Calculations.......................................64

Abstract

The Fermi-Eyges model of electron transport forms the basis of many algorithms used to predict radiation dose distributions in electron beam therapy. However, it has been shown that the errors in the dose distribution calculated using these algorithms may be unacceptably large. Part of the difficulty is due to the inadequacy of the Fermi-Eyges model for the description of electron transport in dense media. Also, in calculating the dose from a single pencil beam, these algorithms assume that inhomogeneities are infinite in their lateral extent.

A modification of the Fermi-Eyges model of electron transport is developed here to overcome the aforementioned weaknesses. The new model, referred to as the restricted scattering model, limits the angular spread of the electrons in order to model the observed saturation in the angular spread of electrons as they penetrate a scattering medium. In this work, dose predictions of both the Fermi-Eyges and restricted scattering models are compared with measured data. It is demonstrated that the restricted scattering model better predicts the observed angular and spatial distribution of electrons for both pencil beams and clinical broad beams.

An integral equation based on Fermi-Eyges theory is developed and incorporated into a numerical algorithm suitable for the calculation of the electron probability density at all points in a heterogeneous medium. It is shown that the algorithm successfully reproduces known analytical results. A modification of the integral equation is then made such that the small angle approximation is relaxed. It is demonstrated that the modified equation qualitatively reproduces the large angle scattering "tails" observed in pencil beam profiles obtained by measurements or Monte Carlo simulations.

Chapter 1

Introduction

1.1 Radiation Therapy with Electron Beams

Fast electrons interact with a scattering medium through various types of interactions: nuclear Coulomb scattering, bremsstrahlung production and electron-electron collisions. Zerby and Keller (1967) discuss these interaction processes in their review of electron transport theory. For electron energies and scattering media of interest in electron beam radiotherapy (energies of 5 to 30 MeV and atomic numbers less than 13), the dominant interaction is that of small-angle nuclear Coulomb scattering.

Electrons have a fairly well defined range since they lose energy nearly continuously through ionization interactions in the scattering medium. As a result, they have the advantage of sparing normal tissues "down-stream" of the target volume. This is their main advantage over high energy photons for use in radiotherapy. Reports on the use of electron beams for radiotherapy appeared more than three decades ago (Loevinger et al.,1961). However, radiotherapy is still dominated by high energy photon beam therapy. One of the impediments to the more wide-spread use of electron beam radiotherapy is the difficulty in predicting the radiation dose distribution in a heterogeneous medium (Brahme,1985).

It is the continuous interaction of the electrons with the scattering medium which gives rise to the difficulty in treatment planning. In contrast to high energy photons which travel in straight paths between discrete interaction sites, electrons follow tortuous paths due to multiple small-angle scattering events. Any model of electron transport applied to radiotherapy treatment planning must take this fact into account and yet remain practical for routine treatment planning purposes.

Most modern electron beam treatment planning systems are based on the Fermi-Eyges model of charged particle transport (Rossi and Greissen,1941; Eyges,1948) which makes the following assumptions:

i) An electron's angle of travel remains small with respect to its initial line of travel over the entire range of the electron.

ii) The sole means of interaction between an electron and the scattering medium is multiple small-angle scattering.

iii) An electron's kinetic energy is a well defined function of depth in the scattering medium.

These may be poor assumptions especially towards the end of the electron range. However, due to its importance in modern electron beam treatment planning, the Fermi-Eyges model will be introduced in detail in section 1.3.

1.2 Linear Angular Scattering Power

Before discussing the Fermi-Eyges model of charged particle transport, it is necessary to introduce the linear angular scattering power (or simply, the scattering power). It is defined as (ICRU, 1984b),

$$k \equiv \frac{d\langle\Theta^2\rangle}{ds} \qquad [1\text{-}1]$$

where $\langle\Theta^2\rangle$ is the mean square angular spread of a beam of electrons and s is path length. Therefore, the scattering power characterizes the increase in the angular spread of electrons as they traverse a scattering medium.

The value of the scattering power depends on both the scattering medium and the kinetic energy of the electrons. Several expressions which give the scattering power exist (ICRU,1984b; Jette,1988; McParland,1989) but the one which will be adopted in the remainder of this thesis is the one given by Jette et al. (1983),

$$k(z) = k_o \cdot \left[\frac{T+1}{T \cdot (T+2)} \right]^2 \qquad [1\text{-}2]$$

where T is the ratio of the electron's kinetic energy to its rest mass and k_o is the scattering constant characteristic of the scattering medium. k_o is given by,

$$k_o = \frac{16\pi e^4}{(m_o c^2)^2} \bullet \Sigma_i \{N_i Z_i (Z_i+1) \bullet \ln(204 Z_i^{-1/3})\} \qquad [1-3]$$

where e is the electron charge, $m_o c^2$ is the electron rest mass and N_i and Z_i are the atom density and atomic number, respectively, of the ith element in the scattering medium. The scattering power given by [1-2] and [1-3] accounts for both electron-electron and electron-nucleus Coulomb scattering (Jette et al.,1983). The summation includes all atomic elements in the scattering medium. Table 1.1 gives the scattering constant, k_o, for several materials.

1.3 The Fermi-Eyges Model of Electron Transport

The time development of the distribution of energetic electrons in a scattering medium is governed by the appropriate Boltzmann equation (Bethe et al.,1938). Using the assumptions (i) to (iii) outlined in section 1.1, a simplified transport equation - the Fermi-Eyges equation - may be derived from the Boltzmann equation (Brahme,1985). However, the approach taken here will be to use a physical argument based on a derivation given by Rossi (1952) to arrive at the Fermi-Eyges transport equation.

Figure 1.1 defines the coordinate axis and the angle of

Table 1.1 Scattering constant, k_o, for several materials.

Material	Scattering Constant* (rad^2/cm)
Water	47.40
Lung*	12.48
Bone*	113.9
Polystyrene	40.92
Carbon (graphite)	67.49
Aluminum	195.2
Copper	1237.
Cadmium	1729.
Lead	3432.

*Calculated from equation [1-3].

*Lung and bone refer to lung equivalent, LN1, and bone equivalent, SB3, respectively (White,1978).

Figure 1.1

Coordinate Axis and Angle of Travel

The positive z-axis indicates increasing depth in the scattering medium and the lateral position of an electron is given by the (x,y) coordinates. $\bar{\Omega}$ represents the direction of travel of an electron. The electron's angle of travel, Θ, is the angle between $\bar{\Omega}$ and the z-axis. The angle between the z-axis and the projection of $\bar{\Omega}$ on the xz-plane is Θ_x. Similarly, Θ_y is the angle between the z-axis and the projection of $\bar{\Omega}$ on the yz-plane.

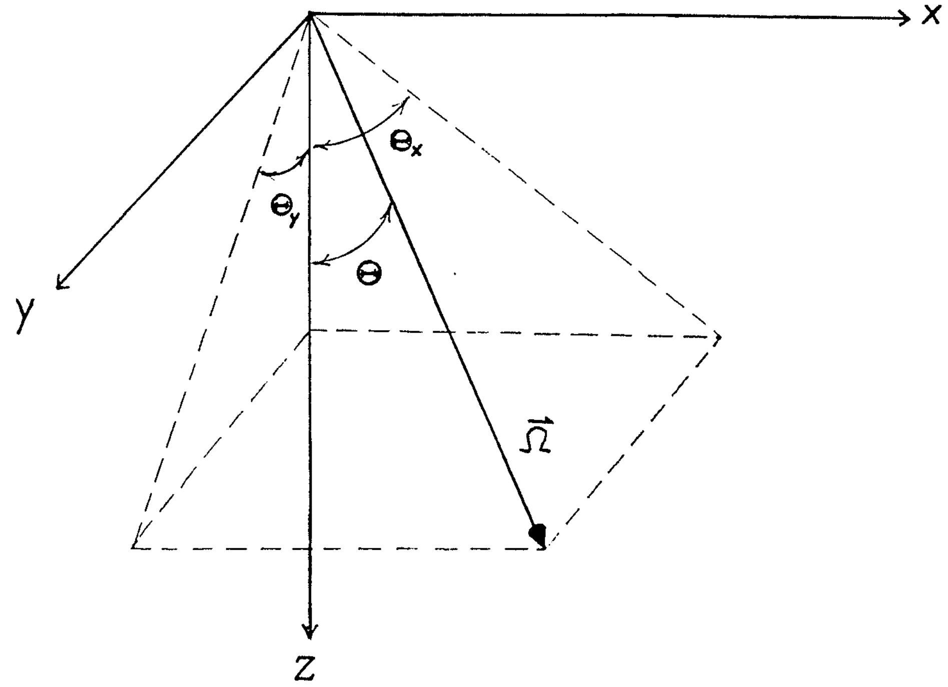
x
y
z
Θ_x
Θ_y
Θ
$\vec{\Omega}$

travel, Θ. The angles, Θ_x and Θ_y, are the angle of travel projected onto the xz-plane and yz-plane respectively. From figure 1.1, it is straightforward to arrive at the relation,

$$\tan^2\Theta = \tan^2\Theta_x + \tan^2\Theta_y \qquad [1-4]$$

If Θ is small, then we may make the approximation $\tan\Theta \approx \Theta$, $\tan\Theta_x \approx \Theta_x$ and $\tan\Theta_y \approx \Theta_y$. Thus, in the small angle approximation, the angles are related by,

$$\Theta^2 = \Theta_x^2 + \Theta_y^2 \qquad [1-5]$$

Let $\langle\Theta^2\rangle$ denote the change in the mean angle of travel of an ensemble of electrons traversing an increment of depth, dz. Since the scattering process is cylindrically symmetric, we must have $\langle\Theta_x^2\rangle = \langle\Theta_y^2\rangle$ and therefore,

$$\langle\Theta^2\rangle = 2\langle\Theta_x^2\rangle = 2\langle\Theta_y^2\rangle = k \cdot dz \qquad [1-6]$$

This last equality follows from the definition of scattering power [1-1] since, if Θ is small, $ds \approx dz$. The relation [1-6] will be needed in the following derivation.

Let $p(\Theta_x', \Theta_y'; \Theta_x, \Theta_y)$ be the probability density for an electron to make a transition from direction (Θ_x, Θ_y) to a new direction (Θ_x', Θ_y') in a depth, dz. Also, let us denote the joint angular-lateral probability density for an electron at depth, z, as $F(z,x,\Theta_x,y,\Theta_y)$. In other words, the probability of finding the electron at depth z with a position in the interval [x,x+dx], [y,y+dy] and with an angle of travel in the interval $[\Theta_x,\Theta_x+d\Theta_x]$, $[\Theta_y,\Theta_y+d\Theta_y]$ is $F(z,x,\Theta_x,y,\Theta_y)dxdyd\Theta_x d\Theta_y$. The electron transport problem is then to find $F(z,x,\Theta_x,y,\Theta_y)$ for all depths, z, in the scattering medium.

First, consider the change in the angular state of an electron as it propagates from z to z+dz. The change in the probability density due electrons scattering out of (Θ_x,Θ_y) is the total scattering probability (i.e. the integral of p over all Θ_x' and Θ_y') multiplied by the probability density at (Θ_x,Θ_y),

$$- F(z,x,\Theta_x,y,\Theta_y)\bullet\int_{-\infty}^{\infty}\int_{-\infty}^{\infty} p(\Theta_x',\Theta_y';\Theta_x,\Theta_y)\, d\Theta_x' d\Theta_y' \tag{1-7}$$

Similarly, the change in probability density due to electrons scattering from other states into (Θ_x,Θ_y) is,

$$\int_{-\infty}^{\infty}\int_{-\infty}^{\infty} F(z,x,\Theta_x',y,\Theta_y')\bullet p(\Theta_x,\Theta_y;\Theta_x',\Theta_y')\, d\Theta_x' d\Theta_y' \tag{1-8}$$

The net change in the probability density due to angular scattering, dF_a, is the sum of [1-7] and [1-8],

$$dF_s = \int_{-\infty}^{\infty}\int_{-\infty}^{\infty} \{F(z,x,\Theta_x',y,\Theta_y') - F(z,x,\Theta_x,\Theta_y)\}$$
$$\bullet p(\Theta_x,\Theta_y;\Theta_x',\Theta_y')\ d\Theta_x' d\Theta_y' \qquad [1\text{-}9]$$

To arrive at [1-9], it has been assumed that $p(\Theta_x',\Theta_y';\Theta_x,\Theta_y) = p(\Theta_x,\Theta_y;\Theta_x',\Theta_y')$.

Assuming that the change in angle is small then the probability density falls off rapidly as Θ_x' or Θ_y' deviate from Θ_x or Θ_y and we can expand $F(z,x,\Theta_x',y,\Theta_y')$ in a Taylor series about (Θ_x,Θ_y),

$$F(z,x,\Theta_x',y,\Theta_y') \approx F(z,x,\Theta_x,y,\Theta_y) + (\Theta_x'-\Theta_x)\bullet\frac{dF}{d\Theta_x}$$
$$+ (\Theta_y'-\Theta_y)\bullet\frac{dF}{d\Theta_y} + \frac{(\Theta_x'-\Theta_x)^2}{2}\bullet\frac{d^2F}{d\Theta_x^2} + \frac{(\Theta_y'-\Theta_y)^2}{2}\bullet\frac{d^2F}{d\Theta_y^2}$$
$$+ (\Theta_x'-\Theta_x)\bullet(\Theta_y'-\Theta_y)\bullet\frac{d^2F}{d\Theta_x d\Theta_y} \qquad [1\text{-}10]$$

Substituting [1-10] into [1-9] and noting that terms containing odd powers of $(\Theta_x'-\Theta_x)$ or $(\Theta_y'-\Theta_y)$ will vanish (since the scattering probability must be symmetric) yields,

$$dF_s = \frac{1}{2}\bullet\frac{d^2F}{d\Theta_x^2}\int_{-\infty}^{\infty}\int_{-\infty}^{\infty}(\Theta_x'-\Theta_x)^2 p(\Theta_x,\Theta_y;\Theta_x',\Theta_y')d\Theta_x'd\Theta_y'$$
$$+ \frac{1}{2}\bullet\frac{d^2F}{d\Theta_y^2}\int_{-\infty}^{\infty}\int_{-\infty}^{\infty}(\Theta_y'-\Theta_y)^2 p(\Theta_x,\Theta_y;\Theta_x',\Theta_y')d\Theta_x'd\Theta_y'$$
$$[1\text{-}11]$$

The first integral is simply $\langle\Theta_x^2\rangle$ and the second is $\langle\Theta_y^2\rangle$. Using [1-6], we get,

$$dF_s = \frac{k \cdot dz}{4} \cdot \left[\frac{d^2F}{d\Theta_x{}^2} + \frac{d^2F}{d\Theta_y{}^2} \right] \qquad [1\text{-}12]$$

Now consider the change in the probability density due to the lateral drift of the electrons as they move from depth z to depth z+dz. Electrons starting with position $(x-\Theta_x dz, y-\Theta_y dz)$ and with direction (Θ_x, Θ_y) arrive at position (x,y). Therefore, as the electrons move, the electrons at (x,y) are replaced by electrons from position $(x-\Theta_x dz, y-\Theta_y dz)$. Denoting the change in probability density due to drift of electrons by dF_d, we have,

$$dF_d = F(z, x-\Theta_x dz, \Theta_x, y-\Theta_y dz, \Theta_y) - F(z, x, \Theta_x, y, \Theta_y) \qquad [1\text{-}13]$$

Expanding the first term on the right hand side to first order in a Taylor series about the point (x,y) yields,

$$dF_d = -\Theta_x dz \cdot \frac{dF}{dx} - \Theta_y dz \cdot \frac{dF}{dy} \qquad [1\text{-}14]$$

The complete change in probability density as the electrons propagate from depth z to depth z+dz is given by summing the two contributions [1-12] and [1-14]. Performing this summation and dividing by dz yields the Fermi-Eyges transport equation,

$$\frac{dF}{dz} = -\Theta_x \bullet \frac{dF}{dx} - \Theta_y \bullet \frac{dF}{dy} + \frac{k(z)}{4} \bullet \left[\frac{d^2F}{d\Theta_x{}^2} + \frac{d^2F}{d\Theta_y{}^2} \right] \qquad [1\text{-}15]$$

Implicit in the derivation above is the assumption that the scattering power, k, does not change in the lateral direction. Therefore, in [1-15], the scattering power is written as a function of z only. This implies that the electron kinetic energy may vary with depth only (see equation [1-2]) and that any inhomogeneities in the scattering medium must be infinite slabs perpendicular to the z-axis.

Since the transport equation [1-15] is separable, it may be written as two equations involving scattering in the xz-plane and scattering in the yz-plane. By writing,

$$F(z,x,\Theta_x,y,\Theta_y) = F_x(z,x,\Theta_x) \bullet F_y(z,y,\Theta_y) \qquad [1\text{-}16]$$

we find that the transport equation governing scattering in the xz-plane is,

$$\frac{dF_x}{dz} = -\Theta_x \bullet \frac{dF_x}{dx} + \frac{k(z)}{4} \bullet \frac{d^2F_x}{d\Theta_x{}^2} \qquad [1\text{-}17]$$

An analogous equation exists for the yz-plane. Because of the separability of the Fermi-Eyges transport equation, only the scattering in the xz-plane will be considered in the present work and the subscript, x, will be dropped for convenience (F_x and Θ_x become F and Θ, respectively).

Using Fourier transform methods, Eyges (1948) has solved [1-17] for an incident point monodirectional pencil beam. More generally, for an incident beam which is jointly Gaussian in x and Θ, the solution of [1-17] is (Brahme et al.,1981),

$$F(z,x,\Theta) = C_1 \bullet \exp\left[C_2 \bullet \left\{\frac{\phi^2}{\sigma_\Theta^2(z)} - 2r \bullet \frac{\blacktriangle x \bullet \phi}{\sigma_\Theta(z) \bullet \sigma_x(z)} + \frac{\blacktriangle x^2}{\sigma_x^2(z)}\right\}\right] \quad [1\text{-}18a]$$

where

$$C_1 = 1/(2\pi\sigma_\Theta\sigma_x(1-r^2)^{1/2}) \quad [1\text{-}18b]$$

$$C_2 = -1/\{2(1-r^2)\} \quad [1\text{-}18c]$$

$$r = r_{x\Theta}(z)/\{\sigma_\Theta(z) \bullet \sigma_x(z)\} \quad [1\text{-}18d]$$

$$\phi = (\Theta - \overline{\Theta}(z)) \quad [1\text{-}18e]$$

$$\blacktriangle x = (x - \overline{x}(z)) \quad [1\text{-}18f]$$

$\overline{\Theta}(z)$ and $\overline{x}(z)$ denote the mean projected angle of travel and mean lateral position at depth z, respectively. $\sigma_\Theta^2(z)$ and $\sigma_x^2(z)$ are the angular and lateral variances, respectively, and $r_{x\Theta}(z)$ is the angular-lateral covariance. These parameters are given at any depth, z, by,

$$\overline{\Theta}(z) = \overline{\Theta}(0) \quad [1\text{-}19a]$$

$$\overline{x}(z) = \overline{x}(0) + \overline{\Theta}(0) \bullet z \quad [1\text{-}19b]$$

$$\sigma_\Theta^2(z) = A_0(z) + \sigma_\Theta^2(0) \quad [1\text{-}19c]$$

$$r_{x\Theta}(z) = A_1(z) + \sigma_\Theta^2(0) \bullet z + r_{x\Theta}(0) \quad [1\text{-}19d]$$

$$\sigma_x^2(z) = A_2(z) + \sigma_\Theta^2(0) \bullet z^2 + 2r_{x\Theta}(0) \bullet z + \sigma_x^2(0) \quad [1\text{-}19e]$$

where the moments, $A_i(z)$ $(i=0,1,2)$, are given by,

$$A_i(z) = \frac{1}{2}\int_0^z k(z')\bullet(z-z')^i dz' \qquad [1\text{-}20]$$

Any broad beam distribution may be thought of as a superposition of a collection of these Gaussian "pencil" beams and this is the basis of pencil beam algorithms for dose calculations in radiotherapy treatment planning.

1.4 Dose Computations Using Pencil Beams

Early methods for electron beam treatment planning involved shifting a standard isodose distribution along ray lines emanating from a "virtual source" (Laughlin,1965; Boone et al.,1967; Almond et al.,1967; Bagne,1976). The assumption implicit in these methods is that the electrons travel in nearly straight paths from the virtual source to the end of their range. As mentioned in section 1.1, electrons do not travel in straight paths and these methods fail to reproduce known effects such as the "hot" and "cold" spots near the edge of an inhomogeneity.

Other methods (Kawachi,1975; Edwards and Coffey,1979) are based on analytical expressions with free parameters which are determined from measured data. However, the reports deal only with homogeneous scattering media and methods for calculations in the presence of inhomogeneities are not discussed. These methods of electron beam treatment planning will not be discussed here. Instead, the discussion will concentrate on pencil beam methods of treatment planning.

Pencil beam methods of treatment planning treat broad beams as a superposition of narrow pencil beams. Figure 1.2 shows schematically how the superposition of pencil beams yields a broad beam distribution in a homogeneous medium. Lillicrap et al. (1975) were one of the first to use the concept of pencil beams explicitly for treatment planning purposes. They measured the dose distributions from narrow electron beams and then used this data to reconstruct various broad beam distributions.

Perry and Holt (1980) present an approximate analytical method of dose calculation in the presence of small inhomogeneities. The method is based on the solution to the Fermi-Eyges transport equation [1-17] but it neglects the electron energy loss in the scattering medium. Hogstrom et al. (1981) have developed a practical pencil beam algorithm for dose calculation by using measured depth dose data as input to the calculations. This approach accounts for dose deposited by secondary electrons and bremsstrahlung photons.

Brahme et al. (1981) and Werner et al. (1982) have modified the Gaussian solution to the transport equation [1-17] to account for the loss of electrons from the forward

Figure 1.2

The Summation of Pencil Beams to Produce a Broad Beam

The figure shows schematically how a broad electron beam may be considered as a superposition of pencil beams. Each pencil beam is assigned a "weight" according to the broad beam profile at the surface of the medium. The individual pencil beam distributions are then calculated using the Fermi-Eyges model and summed to yield the complete broad beam distribution.

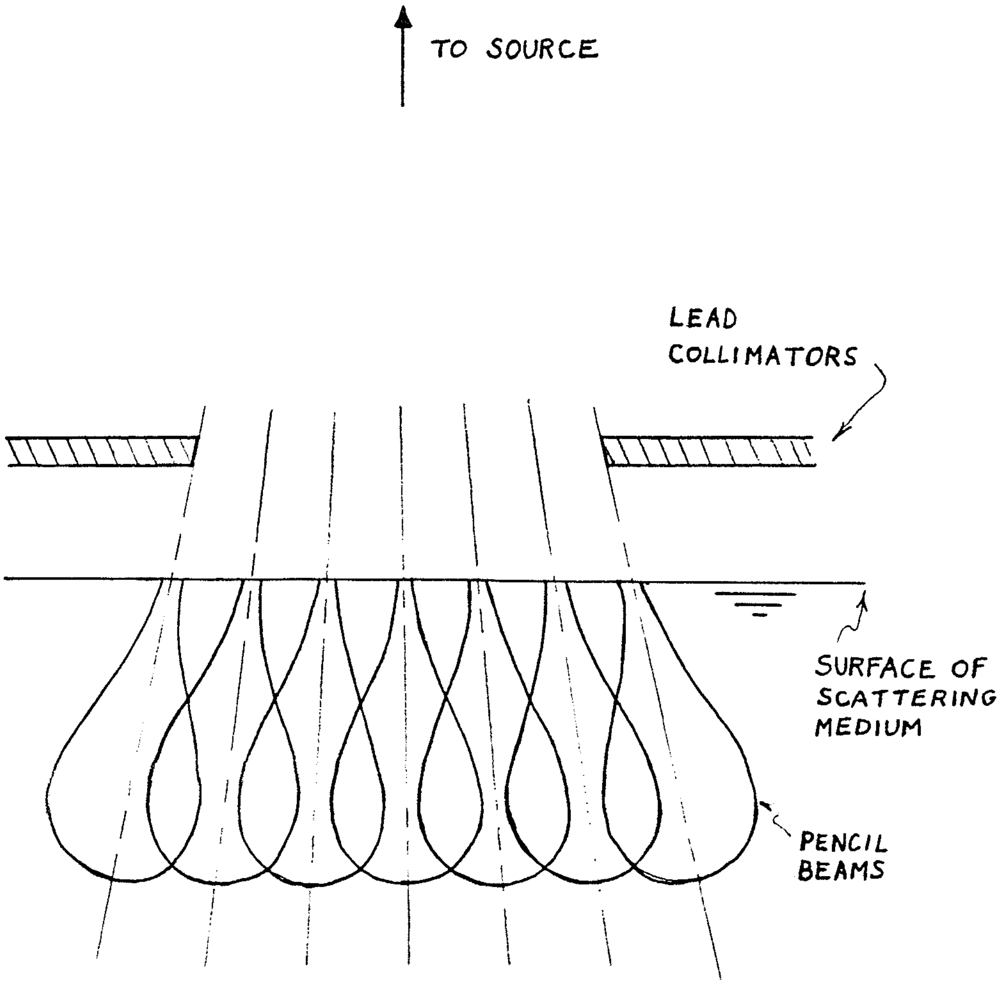
TO SOURCE
LEAD COLLIMATORS
SURFACE OF SCATTERING MEDIUM
PENCIL BEAMS

beam and the resulting decrease in the lateral pencil beam spread. Bruinvis et al. (1983), in their pencil beam dose calculation algorithm, have chosen the Gaussian pencil beam parameters to obtain the best fit to measured data.

It is these analytically based methods mentioned above which are of interest in the present work.

Recall from section 1.3 that the Fermi-Eyges model assumes that the scattering power, k, is a function of depth only. Therefore, the model is restricted to slab-type inhomogeneities in the scattering media (i.e. infinite slabs lying parallel to the xy-plane). In practice, it is assumed that the inhomogeneities are large compared to the width of the pencil beam and that they are well approximated by a slab. Figure 1.3a depicts a single pencil beam passing through an inhomogeneity and figure 1.3b shows the equivalent analytically solvable geometry. All the pencil beams composing a broad beam may be propagated by setting the scattering power at a given depth to be equal to the scattering power on the central axis of the pencil beam. In this way, the complete broad beam distribution may be determined.

The moments method (or pencil beam redefinition algorithm) is a variation on the pencil beam approach (Storchi and Huizenga,1985; Shiu and Hogstrom,1987). The idea of this method is to decompose the beam into a new set of pencil beams at each increment of depth. Thus, the width

Figure 1.3

Equivalent Slab Geometry for Calculations in the Presence of an Inhomogeneity

One of the pencil beams which make up a broad beam is shown passing through an inhomogeneity in an otherwise homogeneous scattering medium (A). The calculation of the pencil beam distribution is performed as if the inhomogeneity were an infinite slab as shown in (B). The thickness of the slab and its depth in the scattering medium are determined by the points at which the central axis of the pencil beam intercepts the boundaries of the inhomogeneity.

(A)

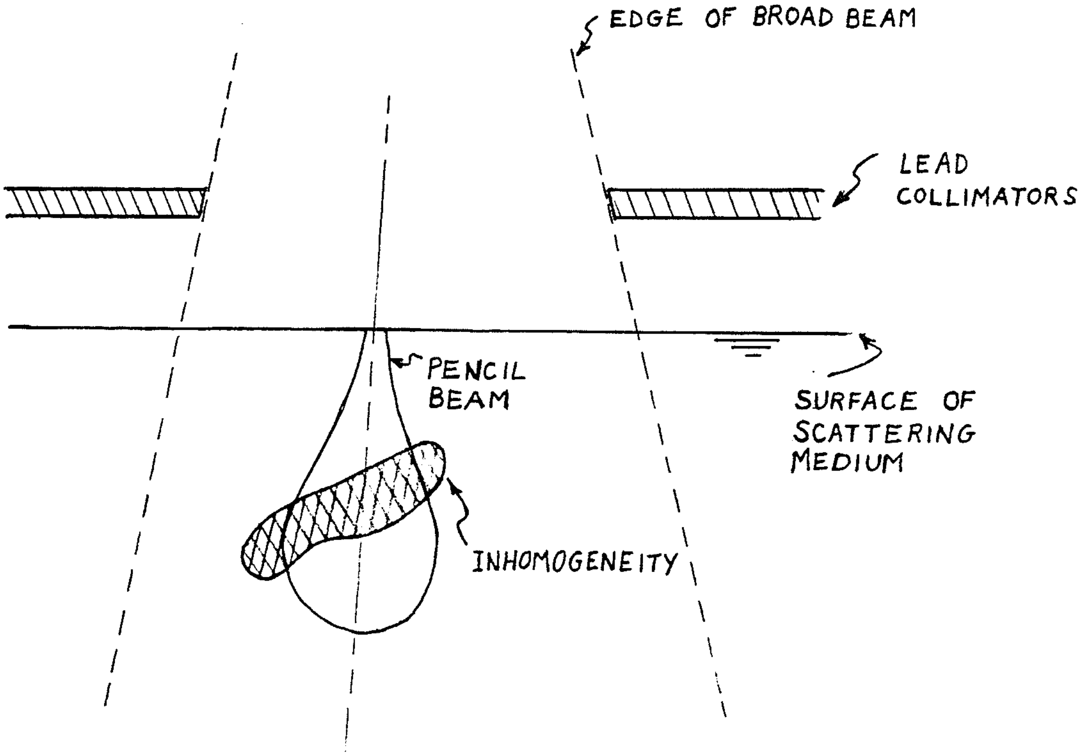
EDGE OF BROAD BEAM
LEAD COLLIMATORS
PENCIL BEAM
SURFACE OF SCATTERING MEDIUM
INHOMOGENEITY

(B)

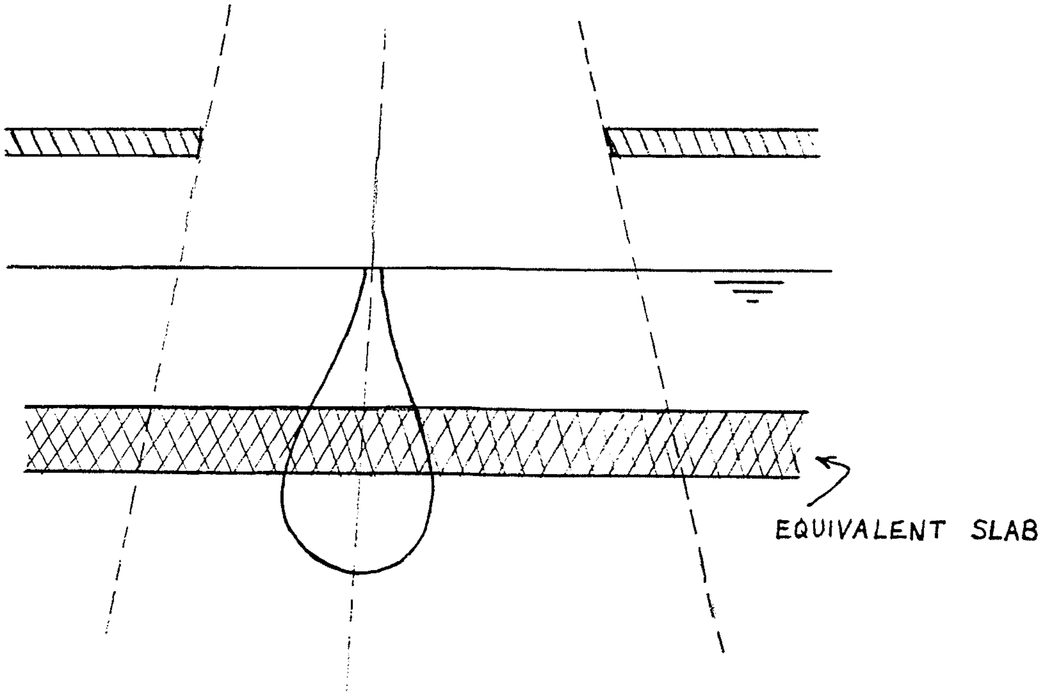
EQUIVALENT SLAB

of the pencil beams remains small compared with the size of inhomogeneities. As a result, the dose distribution near small inhomogeneities is predicted with greater accuracy (Storchi and Huizenga,1985).

However, the original implementation of this approach makes assumptions which are inconsistent with the Fermi-Eyges model (Storchi et al.,1987). Specifically, the method assumes that the angular distribution of electrons at some depth, z, and a fixed lateral point, x, is always Gaussian. However, even for the simple case of a parallel rectangular beam incident on a homogeneous scattering medium, the Fermi-Eyges model predicts a non-Gaussian angular distribution at any fixed lateral point, x. Thus, the moments method cannot be considered as equivalent to the pencil beam methods described above. A numerical method which accounts for the possibility of non-Gaussian angular distributions would be desirable.

1.5 The Purpose of the Present Work

The present work is intended to deal with three separate issues:

(i) The Fermi-Eyges model of electron transport predicts that the electrons' mean square angle of travel and mean square lateral position increase monotonically with depth in the scattering medium and approach infinity as depth approaches the electron range. However, experimental data indicate that the mean square angle of travel reaches a constant value with increasing depth (Roos et al. 1973). Also, the mean square lateral position reaches a maximum value and then decreases towards the end of the electron range (Sandison et al.,1989).

(ii) In the case of small inhomogeneities (where the width of the inhomogeneity is considerably less than the width of the pencil beam) or near the edge of an inhomogeneity, the assumption of slab-geometry is poor. Indeed, it is possible to have unacceptably large errors in the predicted dose distribution for some situations (Shortt et al.,1986; Cygler et al.,1987; Mah et al.,1989).

(iii) The Fermi-Eyges model of electron transport predicts a Gaussian spatial distribution of electrons given an incident point monodirectional pencil beam. However, Monte Carlo generated data (Lax et al.,1983) shows that the distribution has broad non-Gaussian tails due to electrons with large angles of travel.

Chapter 2 presents a modification of the Fermi-Eyges model of electron transport. This new model, called the restricted scattering model, limits the angular spread of the electrons in order to model the observed saturation in the mean square angle of travel as the electrons penetrate the scattering medium. The predictions of the Fermi-Eyges and restricted scattering models for mean square angular spread, mean square lateral position and beam profiles are compared to measured data.

Chapter 3 presents a numerical method of propagating an incident distribution of electrons through an inhomogeneous medium. The numerical method is suitable for dose calculations in the presence of small inhomogeneities. However, unlike the moments method (or pencil beam redefinition algorithm), the numerical method accounts for the possibility of non-Gaussian angular distributions. It is shown that, aside from discretization errors, the method reproduces the analytical predictions of the Fermi-Eyges model.

A modification of the numerical method is then made which relaxes the small angle approximation of the Fermi-Eyges model. It is shown that the modified numerical method qualitatively reproduces the large angle scattering tails seen in Monte Carlo generated data (Lax et al.,1983).

Chapter 2

The Restricted Scattering Model

2.1 The Fermi-Eyges Model: Stochastic Equations Approach

The Fermi-Eyges model of charged particle transport in dense media was discussed in section 1.3. Before introducing the restricted scattering model, however, it will be instructive to re-formulate the Fermi-Eyges model in the language of stochastic equations. The restricted scattering model will then be introduced as a generalization of the Fermi-Eyges model.

As in section 1.3, it is assumed that the only scattering mechanism is that of small angle Coulomb collisions (electron-electron and electron-nucleus collisions). At any given point along the electron's path, the angle of travel is a result of many small independent angular displacements. Therefore, the evolution of the angle of travel along the electron's path is analogous to the time evolution of the position of a particle in Brownian motion.

Brownian motion is well modeled by the Wiener process which will be denoted by $W(z)$. It is a limiting case of the random walk with infinitely small but infinitely many steps and it has the following properties (Karlin and Taylor,1975; Hoel et al.,1984):

(i) $W(a+z)-W(a)$ is normally (Gaussian) distributed with mean 0 and variance z where "a" is a constant.

(ii) The increments $W(z_1)-W(z_2)$, $W(z_3)-W(z_4)$, ..., $W(z_{n-1})-W(z_n)$ are independent random variables if $z_1<z_2\leq z_3<z_4\leq\ldots<z_n$.

(iii) $W(0)=0$ and $W(z)$ is continuous at $z=0$.

If the scattering power is constant with depth then the cumulative angle of travel is given by,

$$\Theta(z) = \Theta(0) + \sqrt{k/2}\bullet W(z) \qquad [2\text{-}1]$$

Since the variance of W(z) is z, the factor $\sqrt{k/2}$ in [2-1] ensures that the mean square angle of travel is kz/2 as predicted by the Fermi model. The quantity $\Theta(0)$ is a random variable representing the initial angle of travel. If the scattering power varies with depth, then it is necessary to write,

$$\Theta(z) = \Theta(0) + \int_0^z \left[\frac{k(z')}{2} \right]^{1/2} dW(z') \qquad [2\text{-}2]$$

Now consider the evolution of the electron's lateral position with depth. For a small angle Θ, the change in lateral position of an electron in an increment of depth, dz, is simply $\Theta\bullet dz$. The lateral position of the electron is the sum of the lateral displacements in each increment of depth. Thus, we write,

$$x(z) = x(0) + \int_0^z \Theta(z')dz' \qquad [2\text{-}3]$$

The quantity x(0) is a random variable representing the electron's initial lateral position. Substituting [2-2] into [2-3] yields,

$$x(z) = x(0) + \Theta(0)\cdot z + \int_0^z \int_0^{z'} \left[\frac{k(z'')}{2} \right]^{½} dW(z'')\, dz' \qquad [2\text{-}4]$$

The stochastic equations [2-2] and [2-4] represent a linear transformation of the Wiener process, W(z). This may be made clear by considering the following identity (Hoel et al.,1984),

$$\int_a^b f(z)dW(z) = f(b)\cdot W(b) - f(a)\cdot W(a) - \int_a^b f'(z)\cdot W(z)dz \qquad [2\text{-}5]$$

The integrals in [2-2] and [2-4] are of the form appearing on the left hand side of [2-5]. The right hand side of [2-5] is clearly a linear transformation of W(z) and it follows that [2-2] and [2-4] are also linear transformations of W(z). Since W(z) is a Gaussian process, [Θ(z),x(z)] must be a jointly Gaussian process and have a probability density of the form [1-18].

The jointly Gaussian probability density, F(z,x,Θ), given by [1-18] is uniquely determined at any given depth, z, by specifying the mean angle of travel, $\overline{\Theta}(z)$, the mean lateral position, $\overline{x}(z)$, the angular variance, $\sigma_{\Theta}^2(z)$, the lateral variance, $\sigma_x^2(z)$, and the angular-lateral covariance, $r_{x\Theta}(z)$. These parameters may be calculated by evaluating the appropriate expectation values,

$$\overline{\Theta}(z) = E\{\Theta(z)\} \qquad [2\text{-}6a]$$

$$\overline{x}(z) = E\{x(z)\} \qquad [2\text{-}6b]$$

$$\sigma_{\Theta}^2(z) = E\{(\Theta(z)-\overline{\Theta}(z))^2\} \qquad [2\text{-}6c]$$

$$r_{x\Theta}(z) = E\{(x(z)-\overline{x}(z))\cdot(\Theta(z)-\overline{\Theta}(z))\} \qquad [2\text{-}6d]$$

$$\sigma_x^2(z) = E\{(x(z)-\overline{x}(z))^2\} \qquad [2\text{-}6e]$$

The symbol, E{ }, denotes the average over the probability space. In appendix 2A, these parameters have been calculated assuming an incident beam which has a jointly Gaussian distribution at the surface of the scattering medium. The results of this calculation are,

$$\overline{\Theta}(z) = \overline{\Theta}(0) \qquad [2\text{-}7a]$$

$$\overline{x}(z) = \overline{x}(0) + \overline{\Theta}(0)\cdot z \qquad [2\text{-}7b]$$

$$\sigma_{\Theta}^2(z) = A_0(z) + \sigma_{\Theta}^2(0) \qquad [2\text{-}7c]$$

$$r_{x\Theta}(z) = A_1(z) + \sigma_{\Theta}^2(0)\cdot z + r_{x\Theta}(0) \qquad [2\text{-}7d]$$

$$\sigma_x^2(z) = A_2(z) + \sigma_{\Theta}^2(0)\cdot z^2 + 2r_{x\Theta}(0)z + \sigma_x^2(0) \qquad [2\text{-}7e]$$

where the moments, $A_i(z)$ (i=0,1,2), are given by,

$$A_i(z) = \frac{1}{2}\int_0^z k(z')\cdot(z-z')^i dz' \qquad [2\text{-}8]$$

In [2-7], $\overline{\Theta}(0)$, $\overline{x}(0)$, $\sigma_\Theta^2(0)$, $r_{x\Theta}(0)$ and $\sigma_x^2(0)$ are the parameters specifying the jointly Gaussian distribution of the incident beam.

The parameters given by [2-7] and [2-8] are identical to those given by [1-19] and [1-20]. This demonstrates the equivalence of the stochastic equations approach and the differential equations approach outlined in section 1.3.

2.2 The Restricted Scattering Model: Stochastic Equations Approach

The Fermi-Eyges model predicts that the mean square angle of travel increases without bound as the electrons penetrate the scattering medium (see [2-7c] and [2-8]). However, it has been experimentally observed (Roos et al.,1973) that the mean square angle of travel approaches a constant value as depth increases. This suggests that electron transport in a dense scattering medium may be better modeled by placing some restriction on the angular scattering of electrons. An analogous problem arises in the description of the velocity distribution of particles in a fluid and this may be modeled using the Ornstein-Uhlenbeck process (Hoel et al.,1984). Therefore, we adopt a model which is mathematically similar to the Ornstein-Uhlenbeck process.

The stochastic equation describing the evolution of the angle of travel now becomes,

$$\Theta(z) = \Theta(0) - \beta\int_0^z \Theta(z')dz' + \int_0^z \left[\frac{k(z')}{2} \right]^{1/2} dW(z') \qquad [2-9]$$

The parameter, β, is a constant which we shall call the restriction parameter. β has units of inverse length. The evolution of the lateral position is given, as in section 2.1, by,

$$x(z) = x(0) + \int_0^z \Theta(z')dz' \qquad [2-10]$$

Equation [2-9] is a generalization of the analogous equation [2-2] in section 2.1 due to the addition of the term involving β. The effect of the additional term is to introduce a scattering bias such that electrons tend to scatter toward smaller angles rather than larger angles. The magnitude of the parameter, β, determines the strength of the scattering bias. Notice that as β or z tend to zero, the stochastic equations [2-2] and [2-4] describing the Fermi-Eyges model are recovered. The determination of β will be discussed later.

In [2-9], $\Theta(z)$ appears on both sides of the equation. By noting the identity,

$$\Theta(z) + \beta\int_0^z \Theta(z')dz' = \exp(-\beta z)\bullet\frac{d}{dz}\Big[\exp(\beta z)\int_0^z \Theta(z')dz'\Big]$$

[2-11]

and after some manipulation, it is possible to rewrite [2-9] as,

$$\Theta(z) = \Theta(0)\bullet\exp(-\beta z) + \int_0^z \Big[\frac{k(z')}{2}\Big]^{1/2} dW(z')$$
$$- \beta\int_0^z \exp(-\beta(z-z'))\int_0^{z'} \Big[\frac{k(z'')}{2}\Big]^{1/2} dW(z'')dz'$$

[2-12]

By using [2-12] in [2-10], it may also be shown that the equation describing the evolution of the lateral position is,

$$x(z) = x(0) + \frac{\Theta(0)}{\beta}\bullet\Big[1 - \exp(-\beta z)\Big]$$
$$+ \int_0^z \exp(-\beta(z-z'))\int_0^{z'} \Big[\frac{k(z'')}{2}\Big]^{1/2} dW(z'')dz'$$

[2-13]

Equations [2-12] and [2-13] show that x(z) and Θ(z) are a linear transformation of the Wiener process. Therefore, as in the case of the Fermi-Eyges model, the electron probability density is the jointly Gaussian density given by [1-19]. As before, the parameters specifying the Gaussian density may be calculated from the appropriate expectation values. These calculations are given in appendix 2B and the results are,

$$\overline{\Theta}(z) = \overline{\Theta}(0)\bullet\exp(-\beta z) \qquad [2\text{-}14a]$$

$$\overline{x}(z) = \overline{x}(0) + \frac{\overline{\Theta}(0)}{\beta}\bullet(1-\exp(-\beta z)) \qquad [2\text{-}14b]$$

$$\sigma_{\Theta}^{2}(z) = A_0(z) + \sigma_{\Theta}^{2}(0)\bullet\exp(-2\beta z) \qquad [2\text{-}14c]$$

$$r_{x\Theta}(z) = A_1(z) + \frac{\sigma_{\Theta}^{2}(0)}{\beta}\bullet\left[\ \exp(-\beta z) - \exp(-2\beta z)\ \right] + r_{x\Theta}(0)\bullet\exp(-\beta z) \qquad [2\text{-}14d]$$

$$\sigma_{x}^{2}(z) = A_2(z) + \frac{\sigma_{\Theta}^{2}(0)}{\beta^{2}}\bullet\left[\ 1 - \exp(-\beta z)\ \right]^{2} + \frac{2r_{x\Theta}(0)}{\beta}\bullet\left[\ 1 - \exp(-\beta z)\ \right] + \sigma_{x}^{2}(0) \qquad [2\text{-}14e]$$

The moments, $A_i(z)$ $(i=0,1,2)$, are now redefined as,

$$A_i(z) = \frac{1}{2}\int_0^z k(z')\bullet\left[\ \frac{\exp(\beta(z-z'))-1}{\beta}\ \right]^{i} \exp(-2\beta(z-z'))\, dz' \qquad [2\text{-}15]$$

It should be noted that the restricted scattering model makes the z-axis its preferred direction. Equation [2-14a] shows that $\overline{\Theta}(z)$ approaches zero as z becomes large regardless of the choice of $\overline{\Theta}(0)$. In other words, the beam will tend to bend to become parallel with the z-axis. Obviously, this is not observed in practice and a solution which makes $\overline{\Theta}(0)$ the preferred direction is more realistic.

Such a solution may be obtained by taking the solution for a normally incident beam (i.e. $\overline{\Theta}(0)=0$) and rotating by the appropriate angle. For a small angle of rotation, ϕ, equations [2-14a] and [2-14b] should be replaced by,

$$\overline{\Theta}(z) = \phi \qquad [2\text{-}16a]$$

$$\overline{x}(z) = \overline{x}(0) + \phi \bullet z \qquad [2\text{-}16b]$$

equations [2-14c] to [2-14e] remain unchanged provided ϕ is small. Thus, an appropriate solution may be obtained for any angle of incidence, ϕ, which is consistent with the small angle approximation.

Some value for the restriction parameter, β, must be determined. In order to find the appropriate value, we first make some observations. First, for a scattering power, k, which remains constant with depth and for an incident point monodirectional pencil beam (i.e. $F(0,x,\Theta)=\delta(x)\delta(\Theta)$), the angular variance is easily obtained from [2-14c] and [2-15],

$$\sigma_{\Theta}^2(z) = A_0(z) = (k/4\beta)\bullet(1-\exp(-2\beta z)) \qquad [2\text{-}17]$$

From this, it may be seen that $\sigma_{\Theta}^2(z)$ approaches a constant value of $k/4\beta$ as z becomes large.

Secondly, as seen in equation [1-6], the mean square angle of travel, $\langle\Theta^2(z)\rangle$, measured for a pencil beam is twice the projected quantity, $\sigma_{\Theta}^2(z)$. i.e.

$$\langle\Theta^2(z)\rangle = 2\sigma_{\Theta}^2(z) \qquad [2\text{-}18]$$

Finally, it is seen experimentally (Roos et al.,1973) that $\langle\Theta^2(z)\rangle$ approaches a constant value close to 0.65 radian^2 for all scattering media and electron energies. Therefore, using [2-17] and [2-18], we arrive at the relation,

$$\beta = k/1.3 \qquad [2\text{-}19]$$

Equation [2-19] applies only when scattering power is not a function of depth. The assumption of a constant scattering power is equivalent to an assumption of negligible energy loss. Obviously, such an assumption is not valid in dense media and it is preferable to incorporate the energy loss of the electrons in the model by allowing the scattering power to vary with depth. A numerical solution which allows both k and β to vary with depth may be constructed as follows.

The electron range may be divided into small increments of depth. Within each increment, the electron energy, scattering power and restriction parameter, β, are held constant. For a Gaussian beam incident on the i^{th} increment, equations [2-14] and [2-15] (with the modification [2-16] if necessary) may be applied assuming constant scattering power to obtain the parameters specifying the distribution at the end of the i^{th} increment. The electron energy, scattering power and restriction parameter (equation [2-19]) may now be recalculated for the

$(i+1)^{th}$ increment. The distribution just calculated for the end of the i^{th} increment now becomes the initial condition for the $(i+1)^{th}$ increment and the distribution at the end of the $(i+1)^{th}$ increment may be calculated. Iterating in this way over many increments, the distribution may be obtained at any depth in the scattering medium. Unless stated otherwise, this is the approach taken in all calculations presented below.

2.3 Comparisons of Mean Square Angle of Travel

Roos et al. (1973) measured, for a range of incident electron energies (5 MeV to 20 MeV) and scattering media (atomic numbers 6 to 82), the angular distribution of electrons as a function of depth for an incident point monodirectional pencil beam. Experimental values of the mean square angle of travel are given for a range of depths and may be used for comparison to the predictions of the Fermi-Eyges model and restricted scattering model.

Under the assumption of constant scattering power and an incident point monodirectional pencil beam, the predictions of the Fermi-Eyges model and restricted scattering model for $\langle\Theta^2(z)\rangle$ may be given in closed analytical form. In particular, the Fermi-Eyges model gives,

$$\langle\Theta^2(z)\rangle = 2\sigma_\theta^2 = kz \qquad [2\text{-}20]$$

The restricted scattering model, on the other hand yields the expression,

$$\langle\Theta^2(z)\rangle = \frac{k}{2\beta}\cdot(1 - \exp(-2\beta z)) \qquad [2\text{-}21]$$

In figure 2.1, the predictions of both [2-20] and [2-21] for $\langle\Theta^2(z)\rangle$ are plotted as a function of kz. Also shown is the data measured by Roos et al. (1973). The curve shows that, for constant scattering power, the restricted scattering model shows the correct saturation behaviour.

As previously mentioned, the case where the scattering power varies with depth is of more interest. Harder's formula may be used to approximate the variation of the average electron energy, $\langle E(z)\rangle$, with depth (ICRU,1984b),

$$\langle E(z)\rangle = \langle E(0)\rangle\cdot(1-z/R_p) \qquad [2\text{-}22]$$

$\langle E(0)\rangle$ is the mean incident electron energy and R_p is the practical range of electrons of energy $\langle E(0)\rangle$. This may be used to find the variation of scattering power, k(z), with depth as described in section 1.2.

Closed form equations may be obtained for the moments, $A_i(z)$, predicted by the Fermi-Eyges model when the energy varies according to Harder's formula (Jette et al.,1983). In the case of the restricted scattering model, the numerical approach described at the end of section 2.2 may

Figure 2.1

Comparison of model predictions of mean square angle of travel for constant scattering power

The mean square angle of travel (denoted $\overline{\Theta^2}$ in this figure) as measured by Roos et al. (1973) is plotted against the dimensionless parameter, kz, for several incident electron energies and scattering media (symbols). The dashed line is the prediction of the Fermi-Eyges model and the solid line indicates the restricted scattering model prediction for a constant scattering power, k. The scattering power was calculated using the initial beam energy.

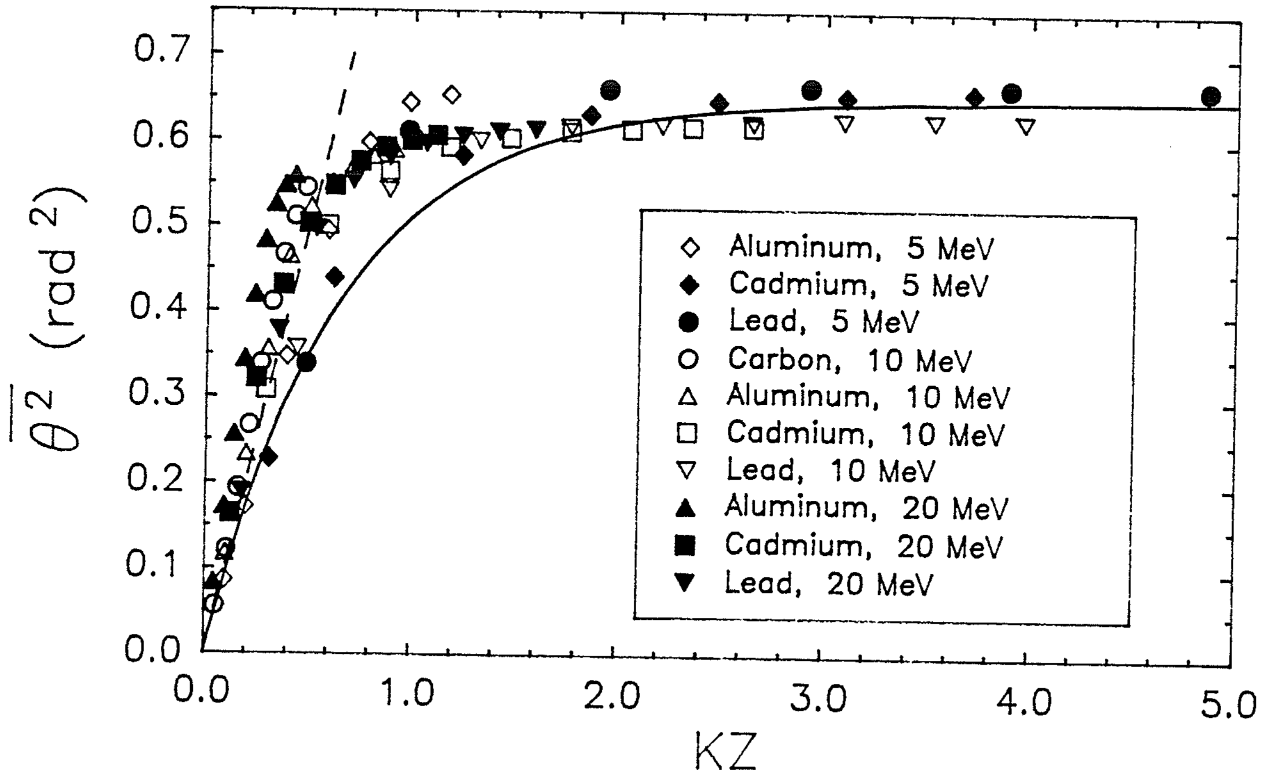
$\overline{\theta^2}$ (rad ^{2})
0.0
0.1
0.2
0.3
0.4
0.5
0.6
0.7
0.0
1.0
2.0
3.0
4.0
5.0
KZ
◇ Aluminum, 5 MeV
◆ Cadmium, 5 MeV
● Lead, 5 MeV
○ Carbon, 10 MeV
△ Aluminum, 10 MeV
□ Cadmium, 10 MeV
▽ Lead, 10 MeV
▲ Aluminum, 20 MeV
■ Cadmium, 20 MeV
▼ Lead, 20 MeV

be used. In the present case, the electron range was divided into 100 depth increments and Harder's formula [2-22] was used to calculate the electron energy at the start of each increment. The predictions of the Fermi-Eyges model and the restricted scattering model are compared to the measured data of Roos et al. (1973) in figures 2.2, 2.3 and 2.4.

2.4 Comparisons of Mean Square Lateral Position

The width of a broad beam penumbra, w(z), is defined as the lateral distance between the intersections of a line tangent at the 50% dose point with the 100% and 0% dose levels. The beam profile at the given depth, z, must be normalized to 100% on the central axis. The penumbra width and mean square pencil beam spread, $\sigma_x^2(z)$, are related by (Sandison and Huda,1988),

$$w(z) = \sqrt{2\pi}\,\sigma_x(z)\bullet\frac{\mathrm{erf}\{a(z)/\sqrt{2}\,\sigma_x(z)\}}{\{1-\exp[-2a^2(z)/\sigma_x^2(z)]\}} \qquad [2\text{-}23]$$

where a(z) is the half-width of the broad beam at depth, z, and erf denotes the error function (Arfken,1970).

Values of $\sigma_x^2(z)$ have been obtained by measuring w(z) for a 10x10 cm^2 field of 16 MeV electrons incident on lung equivalent (LN1) and bone equivalent (SB3) material (White,1978) and for 22 MeV electrons incident on

Figure 2.2

The mean square angle of travel versus depth in carbon

The mean square angle of travel, $\overline{\theta^2}$, is plotted against depth normalized to the continuous slowing down range (defined below), z/R_o, for a 10 MeV point monodirectional pencil beam incident on carbon (graphite). The points (●) are the measured data of Roos et al. (1973). The dashed line and the solid line are the Fermi-Eyges model and restricted scattering model predictions, respectively, using Harder's formula [2-22] to model the variation of electron energy with depth.

The continuous slowing down range is defined as,

$$R_o \equiv \int_0^{E_o} \frac{dE}{S_{tot}(E)}$$

where $S_{tot}(E)$ is the total stopping power in the appropriate medium for electrons of energy, E, and E_o is the energy of the incident electrons.

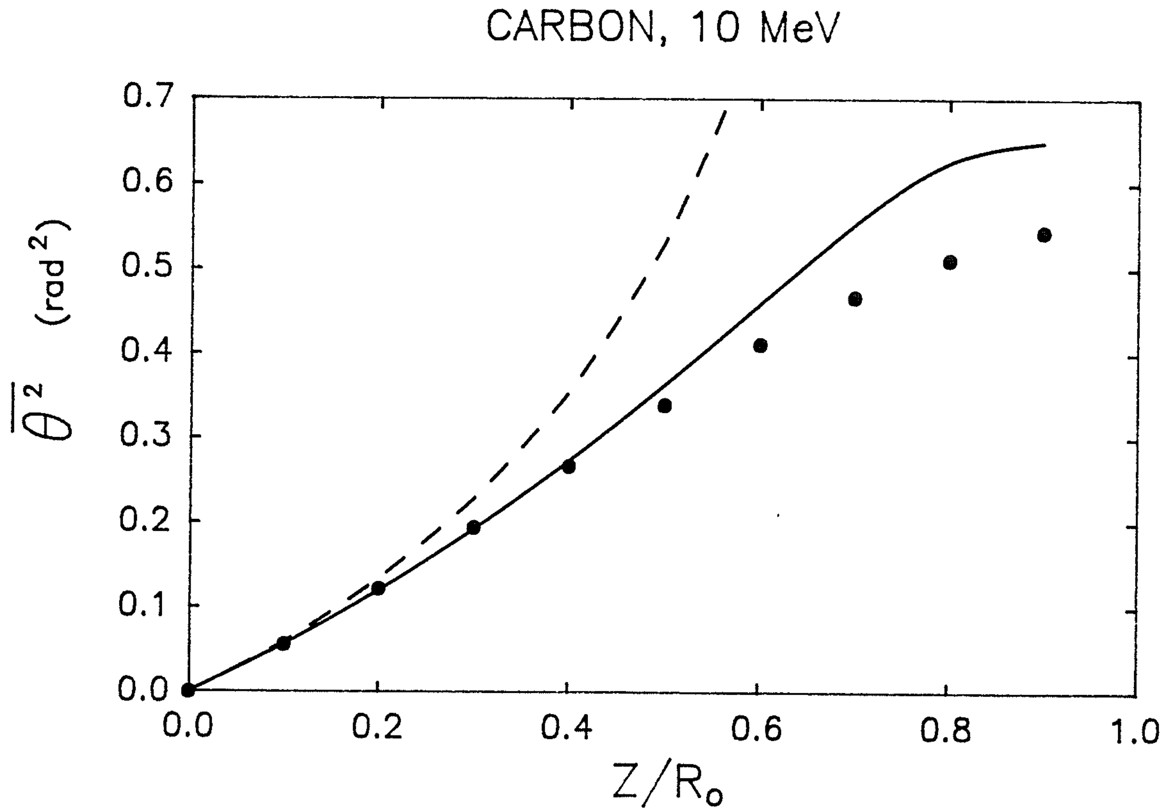CARBON, 10 MeV
$\overline{\theta^2}$ (rad^2)
0.0
0.1
0.2
0.3
0.4
0.5
0.6
0.7
0.0
0.2
0.4
0.6
0.8
1.0
Z/R$_o$

Figure 2.3

The mean square angle of travel versus depth in aluminum

The mean square angle of travel, $\overrightarrow{\Theta^2}$, is plotted against depth normalized to the continuous slowing down range, z/R_o, for a 10 MeV point monodirectional pencil beam incident on aluminum. The points (●) are the measured data of Roos et al. (1973). The dashed line and the solid line are the Fermi-Eyges model and restricted scattering model predictions, respectively, using Harder's formula [2-22] to model the variation of electron energy with depth.

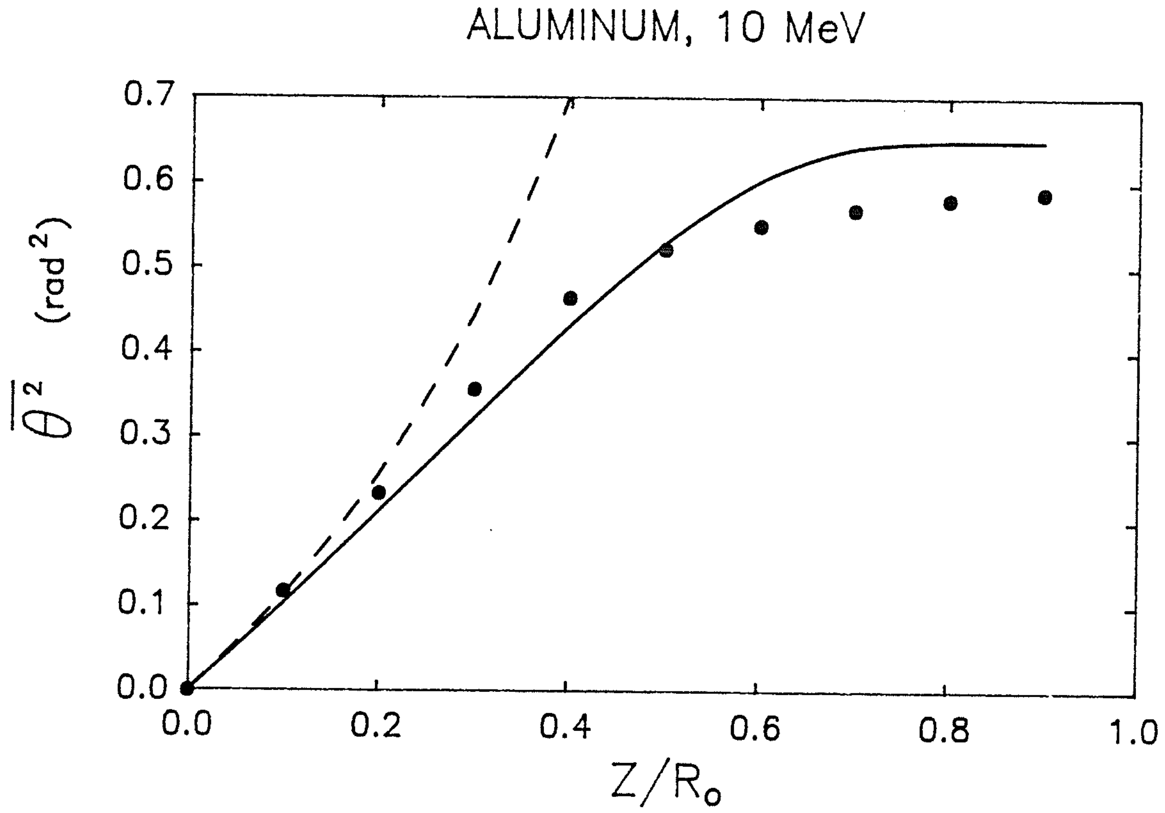
ALUMINUM, 10 MeV
$\overline{\theta^2}$ (rad^2)
0.0
0.1
0.2
0.3
0.4
0.5
0.6
0.7
0.0
0.2
0.4
0.6
0.8
1.0
Z/R_o

Figure 2.4

The mean square angle of travel versus depth in lead

The mean square angle of travel, $\overline{\Theta^2}$, is plotted against depth normalized to the continuous slowing down range, z/R_o, for a 10 MeV point monodirectional pencil beam incident on lead. The points (●) are the measured data of Roos et al. (1973). The dashed line and the solid line are the Fermi-Eyges model and restricted scattering model predictions, respectively, using Harder's formula [2-22] to model the variation of electron energy with depth.

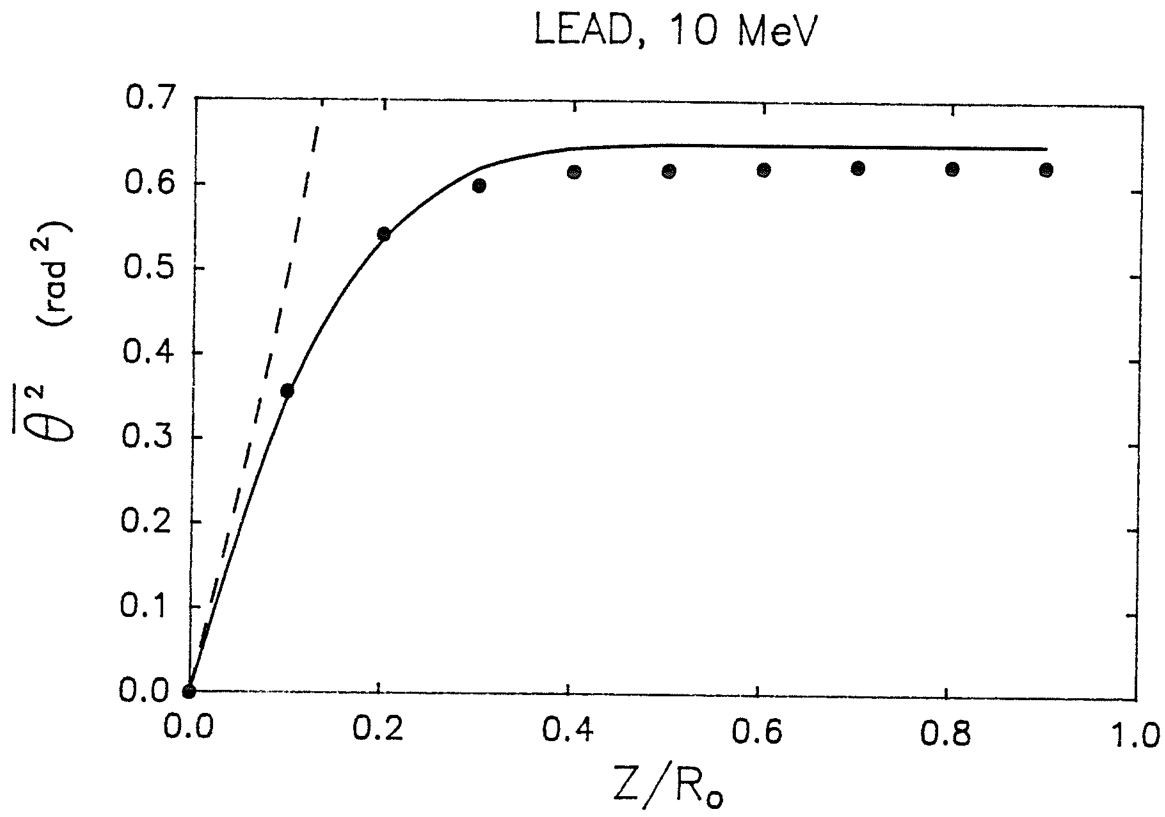
LEAD, 10 MeV
0.7
0.6
0.5
0.4
0.3
0.2
0.1
0.0
$\overline{\theta^2}$ (rad^2)
0.0
0.2
0.4
0.6
0.8
1.0
Z/R_o

polystyrene. The electron beams were produced by a Sagittaire Therac 40 linear accelerator and the measurements were accomplished using film (Kodak Industrex M) mounted parallel to the beam axis in a homogeneous phantom. The method has been described in detail elsewhere (Sandison et al.,1989).

The predictions of the Fermi-Eyges model and the restricted scattering model are compared to the measured data in figures 2.5, 2.6 and 2.7. Harder's formula [2-22] has been used to calculate the electron energy loss. In the case of the restricted scattering model, the numerical method described at the end of section 2.2 was used to perform the calculations.

2.5 Clinical Beam Profiles

It is straightforward to integrate Gaussian pencil beams across a broad beam area to obtain the predicted broad beam probability density in a homogeneous scattering medium,

$$F(z,x,y) = \frac{1}{4}\cdot\left[\frac{SSD}{SSD+z}\right]^2 \cdot[\mathrm{erf}\{A(a,x)\} - \mathrm{erf}\{A(-a,x)\}] \cdot[\mathrm{erf}\{A(b,y)\} - \mathrm{erf}\{A(-b,y)\}] \qquad [2\text{-}24a]$$

where the function, A(u,v), is given by,

Figure 2.5

The root mean square lateral position versus depth in lung

The root mean square lateral position, σ ($=\sqrt{\sigma_x^2}$), is plotted against depth, z, for a 16 MeV point monodirectional pencil beam incident on a lung equivalent medium. Both σ and z have been normalized to the continuous slowing down range, R_o. The points (●) are the measured data obtained from broad beam penumbra (see text). The dashed line and the solid line are the Fermi-Eyges model and restricted scattering model predictions, respectively, using Harder's formula [2-22] to model the variation of electron energy with depth.

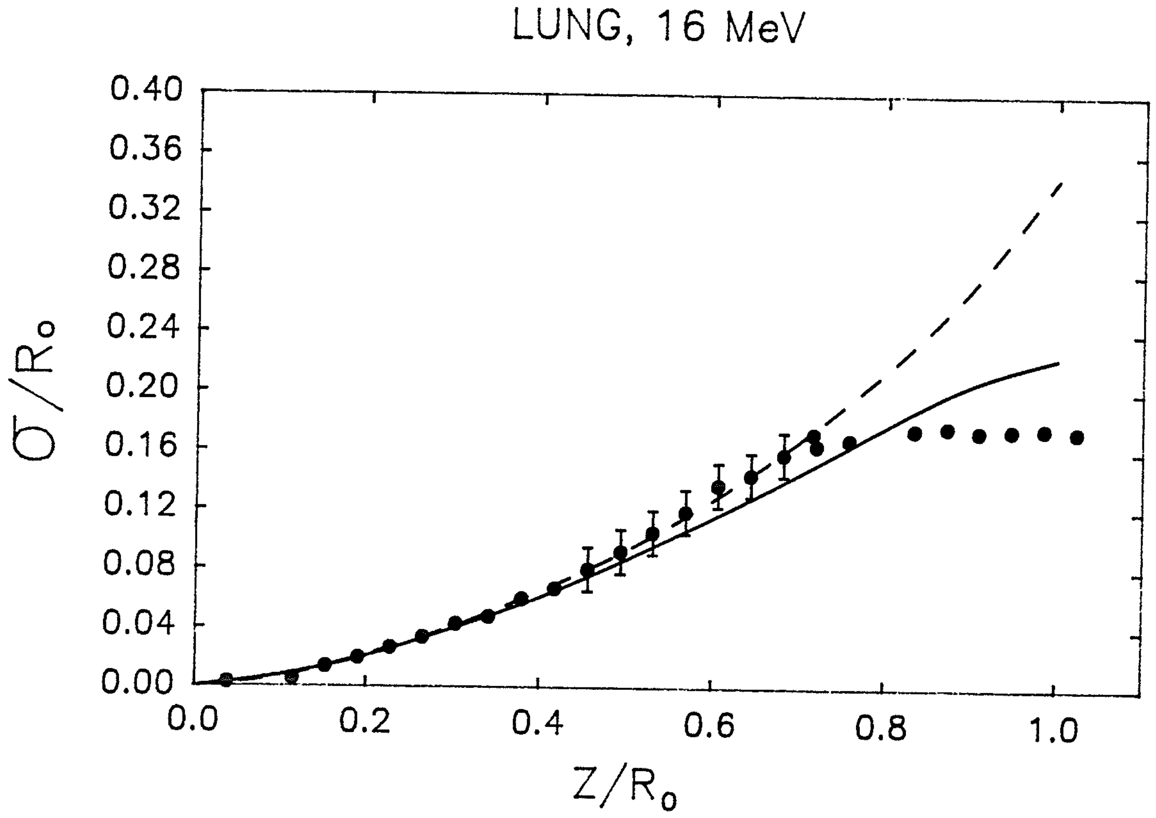
LUNG, 16 MeV
σ/R₀
Z/R₀
0.00
0.04
0.08
0.12
0.16
0.20
0.24
0.28
0.32
0.36
0.40
0.0
0.2
0.4
0.6
0.8
1.0

Figure 2.6

The root mean square lateral position versus depth in bone

The root mean square lateral position, σ $(=\sqrt{\overline{\sigma_x^2}})$, is plotted against depth, z, for a 16 MeV point monodirectional pencil beam incident on a bone equivalent medium. Both σ and z have been normalized to the continuous slowing down range, R_o. The points (●) are the measured data obtained from broad beam penumbra (see text). The dashed line and the solid line are the Fermi-Eyges model and restricted scattering model predictions, respectively, using Harder's formula [2-22] to model the variation of electron energy with depth.

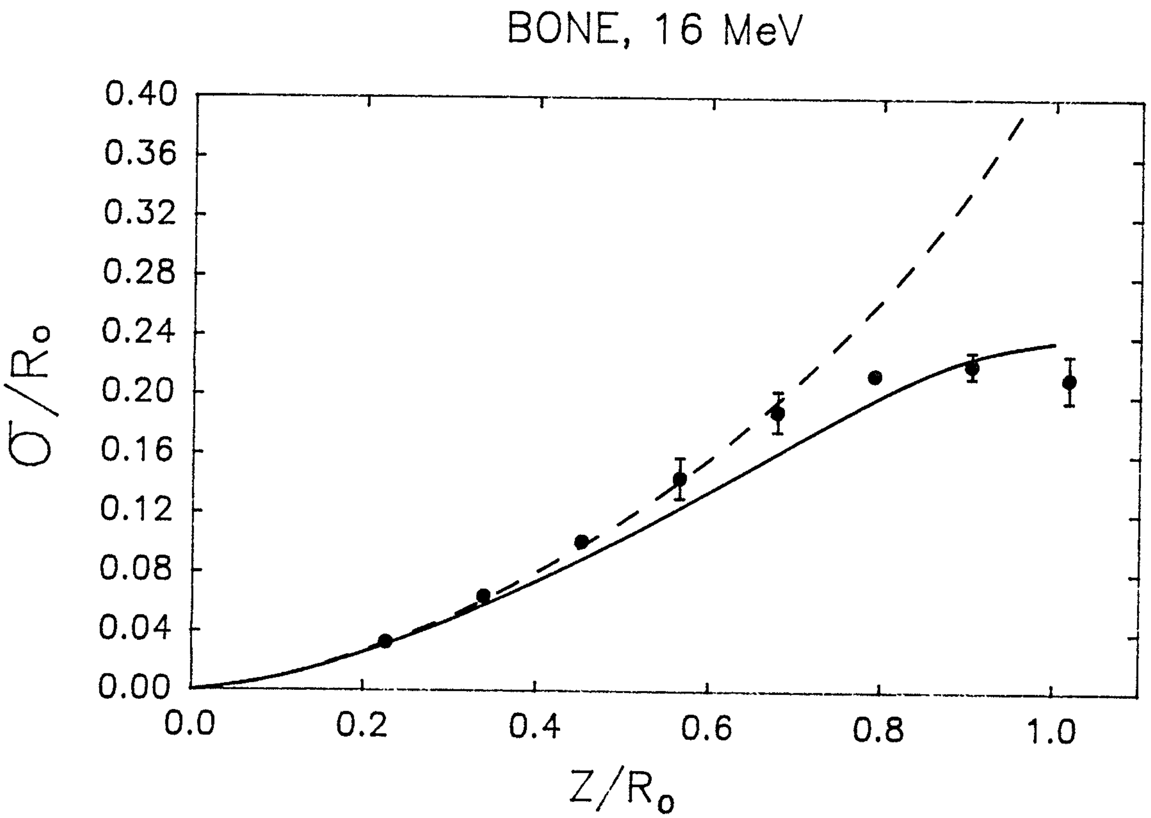

BONE, 16 MeV
0.40
0.36
0.32
0.28
0.24
0.20
0.16
0.12
0.08
0.04
0.00
σ/R₀
0.0
0.2
0.4
0.6
0.8
1.0
Z/R₀

Figure 2.7

The root mean square lateral position versus depth in polystyrene

The root mean square lateral position, σ ($=\sqrt{\sigma_x^2}$), is plotted against depth, z, for a 22 MeV point monodirectional pencil beam incident on polystyrene. Both σ and z have been normalized to the continuous slowing down range, R_o. The points (●) are the measured data obtained from broad beam penumbra (see text). The dashed line and the solid line are the Fermi-Eyges model and restricted scattering model predictions, respectively, using Harder's formula [2-22] to model the variation of electron energy with depth. Error bars are not visible on the measured points indicating that the estimated error is less than or equal to the size of the points.

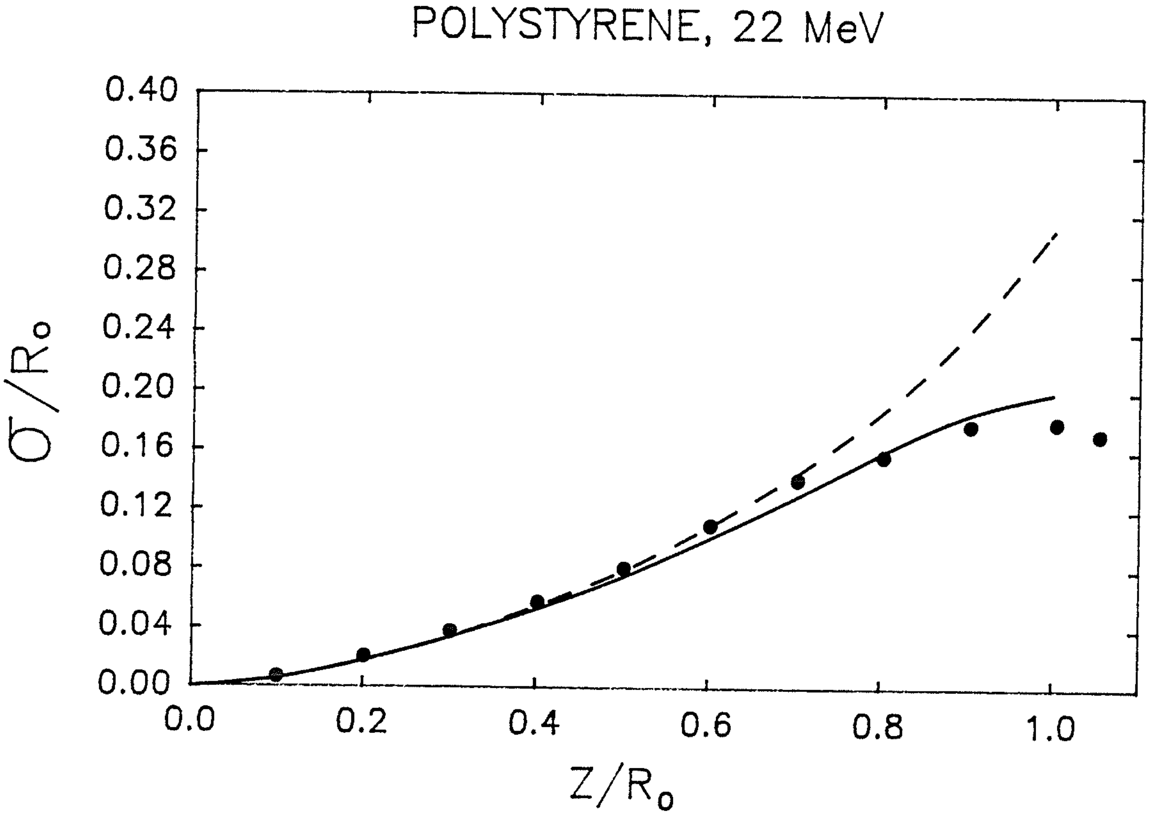
POLYSTYRENE, 22 MeV
σ/R₀
0.40
0.36
0.32
0.28
0.24
0.20
0.16
0.12
0.08
0.04
0.00
0.0
0.2
0.4
0.6
0.8
1.0
Z/R₀

$$A(u,v) = \frac{\left[u \cdot \left[\frac{SSD + z}{SSD} \right] - v \right]}{\sqrt{2}\, \sigma_x(z)} \qquad [2\text{-}24b]$$

SSD is the source-to-surface distance and a and b are the half-field width and length, respectively, at the surface of the scattering medium. At a given depth, z, the probability of finding an electron with x coordinate in the interval [x,x+dx] and y coordinate in the interval [y,y+dy] is F(z,x,y)dxdy.

The distribution given by [2-24] is valid for both the Fermi-Eyges model and the restricted scattering model provided the modification [2-16] is employed in the restricted scattering model (i.e. the solution for a normally incident pencil beam is rotated by an appropriate angle). The only difference between the two models is the expression used for $\sigma_x^2(z)$: equation [2-7e] for the Fermi-Eyges model and equation [2-14e] for the restricted scattering model. However, for a clinical beam, the pencil beam parameters, $\sigma_\theta^2(0)$, $r_{x\theta}(0)$ and $\sigma_x^2(0)$, have non-zero values and they must be determined in order to find $\sigma_x^2(z)$. Methods to determine these parameters for a magnetically scanned beam exist in the literature (Huizenga and Storchi,1987; Sandison and Huda,1988).

In order to compare the predicted broad beam probability density with measured data, it has been assumed that, for a set depth z in a homogeneous medium, the probability density is proportional to the radiation dose. Therefore, measured dose profiles may be compared to the theoretical predictions of probability density by normalizing the measured dose profile and the predicted probability density to the same value (eg. 100%) on the central axis.

Using the same method as in section 2.4, dose profiles were measured for a 10x10 cm^2, 16 MeV beam in lung (LN1) and bone (SB3) equivalent media (White,1978) and for a 10x10 cm^2, 22 MeV beam in polystyrene. These measurements have been compared to beam profiles calculated using the Fermi-Eyges and restricted scattering models in figures 2.8, 2.9 and 2.10.

2.6 Discussion

The observation from measured angular distribution data (Roos et al.,1973) that the mean square angle of travel, $\langle\Theta^2(z)\rangle$, saturates with depth is the motivation for the modification of the Fermi-Eyges model. As shown in figures 2.1, 2.2, 2.3 and 2.4, the restricted scattering model successfully predicts this saturation for both constant and variable scattering power, k(z). When scattering power is allowed to vary with depth in the scattering medium, reasonable agreement is obtained with the measured angular distribution data at all depths for a wide range of incident electron energies (5 to 20 MeV) and scattering media (atomic

Figure 2.8

Broad beam profile for 16 MeV electrons in lung

A broad beam profile is shown at 22 cm depth in a lung equivalent medium (practical range, R_p, of 27.9 cm). The beam has dimensions 10x10 cm^2 at 100 cm SSD (source-to-surface distance) with an incident energy of 16 MeV. The points (●) indicate data measured using film as described in the text. The dashed line and the solid line are the Fermi-Eyges and restricted scattering model predictions, respectively. Harder's formula [2-22] was used to model the variation of electron energy with depth.

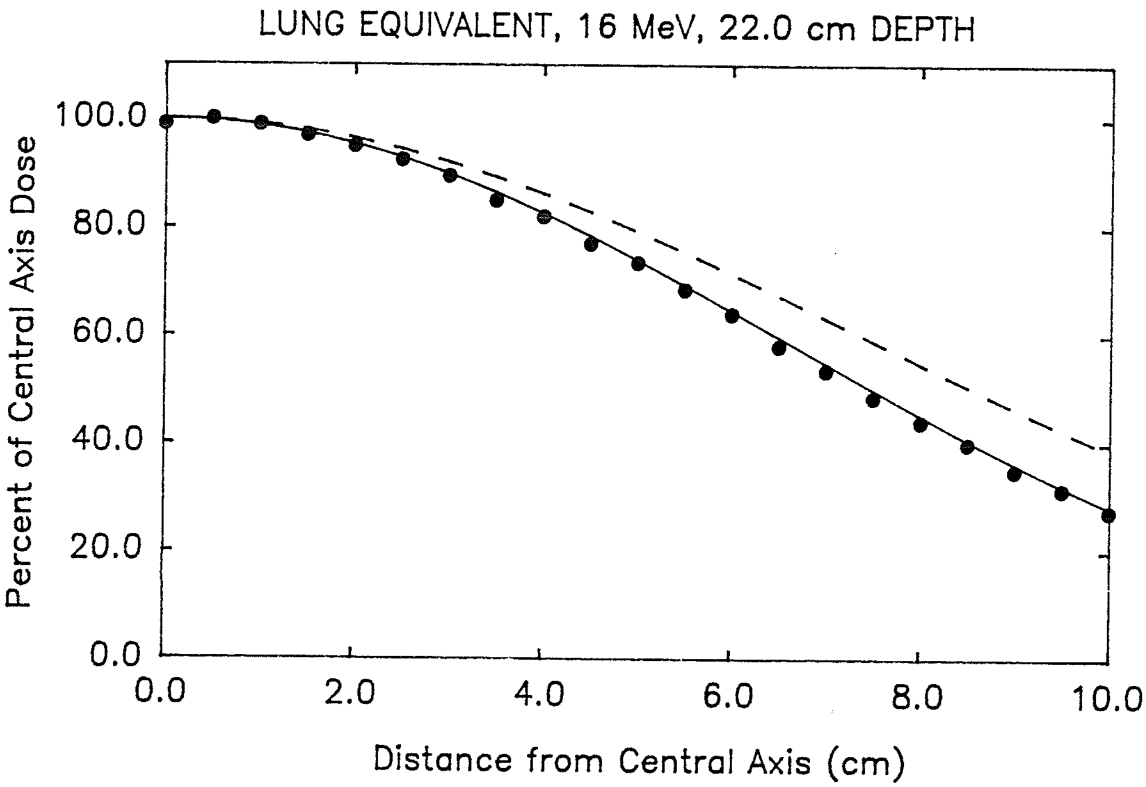
LUNG EQUIVALENT, 16 MeV, 22.0 cm DEPTH
Percent of Central Axis Dose
100.0
80.0
60.0
40.0
20.0
0.0
0.0
2.0
4.0
6.0
8.0
10.0
Distance from Central Axis (cm)

Figure 2.9

Broad beam profile for 16 MeV electrons in bone

A broad beam profile is shown at 4 cm depth in a bone equivalent medium (practical range, R_p, of 4.67 cm). The beam has dimensions 10x10 cm^2 at 100 cm SSD (source-to-surface distance) with an incident energy of 16 MeV. The points (●) indicate data measured using film as described in the text. The dashed line and the solid line are the Fermi-Eyges and restricted scattering model predictions, respectively. Harder's formula [2-22] was used to model the variation of electron energy with depth.

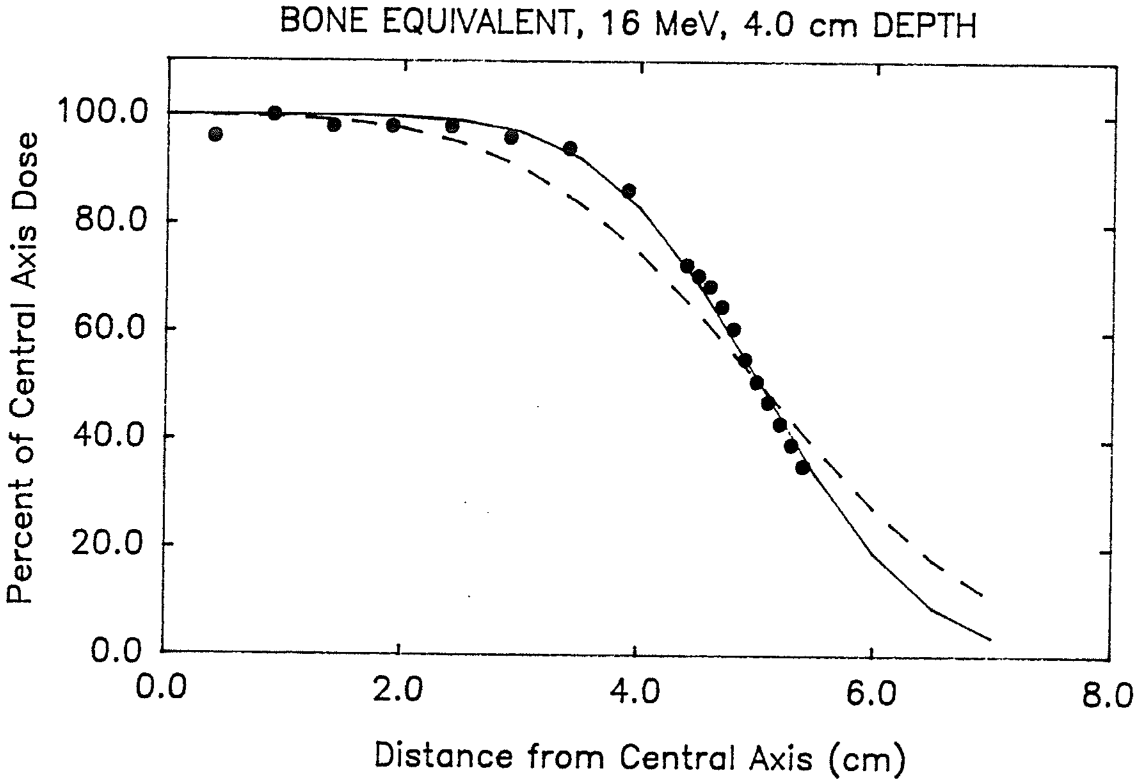
BONE EQUIVALENT, 16 MeV, 4.0 cm DEPTH
Percent of Central Axis Dose
100.0
80.0
60.0
40.0
20.0
0.0
0.0
2.0
4.0
6.0
8.0
Distance from Central Axis (cm)

Figure 2.10

Broad beam profile for 22 MeV electrons in polystyrene

A broad beam profile is shown at 9.6 cm depth in polystyrene (practical range, R_p, of 10.46 cm). The beam has dimensions 10x10 cm^2 at 100 cm SSD (source-to-surface distance) with an incident energy of 16 MeV. The points (●) indicate data measured using film as described in the text. The dashed line and the solid line are the Fermi-Eyges and restricted scattering model predictions, respectively. Harder's formula [2-22] was used to model the variation of electron energy with depth.

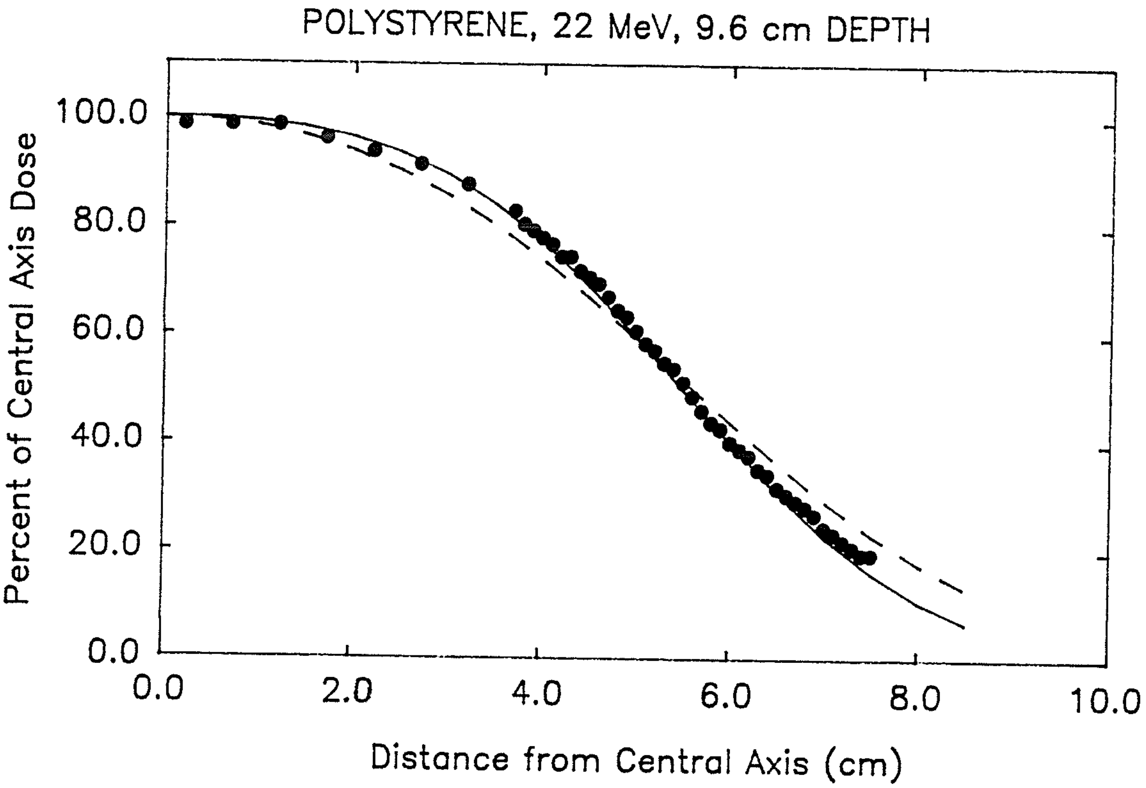
POLYSTYRENE, 22 MeV, 9.6 cm DEPTH
Percent of Central Axis Dose
100.0
80.0
60.0
40.0
20.0
0.0
0.0
2.0
4.0
6.0
8.0
10.0
Distance from Central Axis (cm)

numbers ranging from 6 to 82). This agreement is indicated in figures 2.2, 2.3 and 2.4 for a 10 MeV point monodirectional pencil beam incident on carbon, aluminum and lead.

It was noted earlier that the lateral scattering process, x(z), is an integral of the angular scattering process, $\Theta(z)$, so we expect that an improvement in the prediction of the variation of $\langle\Theta^2(z)\rangle$ with depth will coincide with an improvement in the prediction of the variation in the lateral pencil beam spread with depth. In figures 2.5, 2.6 and 2.7, it can be seen that both the Fermi-Eyges and restricted scattering models agree closely with the measured lateral spread of electrons up to about 0.7 of the continuous slowing down range. The curve predicted by the restricted scattering model lies slightly below that predicted by the Fermi-Eyges model but, in general, both curves lie within the experimental error. However, the restricted scattering model does provide a significant improvement over the Fermi-Eyges model deeper in the scattering medium. As a result of this improvement, the restricted scattering model gives better predictions of clinical beam profiles at depths greater than 0.7 of the csda range as indicated in figures 2.8, 2.9 and 2.10.

Some empirical modifications to the pencil beam spread, $\sigma_x^2(z)$, predicted by the Fermi-Eyges model have been suggested (Werner et al.,1982; Lax et al,1983). For certain beam energies and scattering media these give good agreement with the measured pencil beam spread, $\sigma_x^2(z)$. However, it has been shown (Sandison et al.,1989) that the modifications are not applicable to the entire range of energies and scattering media of clinical interest. The modification of $\sigma_x^2(z)$ suggested by Lax et al. (1983) may be generalized for use at any energy and in any scattering medium by introducing 3 parameters which may be determined by a fit to measured data (Sandison et al.,1989). The resulting values of the parameters depend on the scattering medium and, possibly, beam energy. Therefore, this approach is inconvenient for dose calculations in heterogeneous media. The restricted scattering model gives improved fits to measured pencil beam spread, $\sigma_x^2(z)$, for the entire range of beam energies and scattering media investigated. Also, no additional parameters are required since the restriction parameter, ß, may be easily determined from the linear scattering power, k(z), using equation [2-19].

Pencil beam dose calculation algorithms currently in clinical use are based on Gaussian pencil beams and the restricted scattering model retains the Gaussian features of the Fermi-Eyges model. Therefore, the application of the restricted scattering model is straightforward since it can be directly incorporated into existing pencil beam dose computation algorithms.

2.7 Conclusion

The restricted scattering model is successful in predicting the variation of the mean square angle of travel of the electrons with depth over the entire electron range for incident electron energies from 5 MeV to 20 MeV in various scattering media with atomic numbers from 6 to 82. An improvement over the Fermi-Eyges model is obtained in the prediction of the variation of the lateral pencil beam spread for depths greater than about 0.7 of the electron range. The improvement in the prediction of the pencil beam spread leads to an improvement in the prediction of penumbra shape for clinical beams in homogeneous scattering media. Also, since the restricted scattering model retains the Gaussian features exhibited by the Fermi-Eyges model and no additional measured data is required, it may be readily incorporated into existing dose computation algorithms.

Appendix 2A

In this appendix, the moments specifying the jointly Gaussian probability density predicted by the Fermi-Eyges model are explicitly calculated. It is assumed that $x(0)$ and $\Theta(0)$ are random variables which represent the initial pencil beam position and angle, respectively, and that they have a jointly Gaussian probability density.

As mentioned in section 2.1, the moments are given by the appropriate expectation values. In order to evaluate these expectation values, we use the following properties of the Wiener process (Hoel et al.,1984),

$$E\{ \int_0^a f(z)\, dW(z) \} = 0 \qquad [2A-1]$$

and,

$$E\{ \left[\int_0^a f(z)\, dW(z) \right] \cdot \left[\int_0^b g(z)\, dW(z) \right] \} = \int_0^{\min(a,b)} f(z) \cdot g(z)\, dz \qquad [2A-2]$$

Using [2-2] and the properties [2A-1] and [2A-2], the mean angle of travel is,

$$\overline{\Theta}(z) = E\{\Theta(z)\} = \overline{\Theta}(0) \qquad [2A-3]$$

Also, from [2-4], the mean lateral position is,

$$\overline{x}(z) = E\{x(z)\} = \overline{x}(0) + \overline{\Theta}(0)\cdot z \qquad [2A-4]$$

The interchangeability of the expectation and integration with respect to z has been used to arrive at [2A-4].

Now consider the mean square angle of travel, $\sigma_\Theta^2(z)$. Using [2-2],

$$\begin{aligned}\sigma_\Theta^2(z) &= E\{[\Theta(z)-\overline{\Theta}(z)]^2\}\\ &= E\{[\Theta(z)-\overline{\Theta}(0)]^2\}\\ &= E\{\left[\Theta(0) + \int_0^z \left[\frac{k(z')}{2}\right]^{1/2} dW(z') - \overline{\Theta}(0)\right]^2\}\end{aligned}$$

The Wiener process, W(z), and the initial random variables are independent. If the initial mean square angle of travel is $\sigma_\Theta^2(0)$, then we have,

$$\sigma_\Theta^2(z) = \sigma_\Theta^2(0) + \frac{1}{2}\int_0^z k(z')dz' \qquad [2A-6]$$

Similarly, the covariance is given by,

$$\begin{aligned}r_{x\Theta}(z) &= E\{[x(z)-\overline{x}(z)]\cdot[\Theta(z)-\overline{\Theta}(z)]\}\\ &= r_{x\Theta}(0) + \sigma_\Theta^2(0)\cdot z + \frac{1}{2}\int_0^z k(z')\cdot(z-z')dz'\end{aligned}$$

[2A-7]

Finally, the mean square lateral position is,

$$\sigma_{\Theta}^{2}(z) = E\{[x(z)-\overline{x}(z)]^{2}\}$$

$$= \sigma_{x}^{2}(0) + 2r_{x\Theta}(0)z + \sigma_{\Theta}^{2}(0)z^{2} + \frac{1}{2}\int_{0}^{z} k(z')\cdot(z-z')^{2}dz'$$

[2A-8]

To summarize, the parameters specifying the jointly Gaussian probability density predicted by the Fermi-Eyges model are,

$$\overline{\Theta}(z) = \overline{\Theta}(0) \qquad [2A\text{-}9a]$$

$$\overline{x}(z) = \overline{x}(0) + \overline{\Theta}(0)\cdot z \qquad [2A\text{-}9b]$$

$$\sigma_{\Theta}^{2}(z) = \sigma_{\Theta}^{2}(0) + A_{0}(z) \qquad [2A\text{-}9c]$$

$$r_{x\Theta}(z) = r_{x\Theta}(0) + \sigma_{\Theta}^{2}(0)\cdot z + A_{1}(z) \qquad [2A\text{-}9d]$$

$$\sigma_{x}^{2}(z) = \sigma_{x}^{2}(0) + 2r_{x\Theta}(0)\cdot z + \sigma_{\Theta}^{2}(0)\cdot z^{2} + A_{2}(z) \qquad [2A\text{-}9e]$$

where the moments, $A_i(z)$ $(i=0,1,2)$, are given by,

$$A_{i}(z) = \frac{1}{2}\int_{0}^{z} k(z')\cdot(z-z')^{i}dz' \qquad [2A\text{-}10]$$

These are the parameters [2-7] given in section 2.1.

Appendix 2B

In this appendix, the parameters specifying the jointly Gaussian probability density predicted by the restricted scattering model are explicitly calculated. It is assumed that $x(0)$ and $\Theta(0)$ are random variables which represent the initial pencil beam position and angle, respectively, and that they have a jointly Gaussian probability density. The calculations are exactly analogous to those performed for the Fermi-Eyges model and are based on the properties of the Wiener process [2A-1] and [2A-2].

The stochastic processes $\Theta(z)$ and $x(z)$ are related to the Wiener process, $W(z)$, by [2-12] and [2-13]. The mean angle of travel and the mean lateral position are given by,

$$\begin{aligned} \overline{\Theta}(z) &= E\{\Theta(z)\} \\ &= \overline{\Theta}(0)\cdot\exp(-\beta z) \end{aligned} \qquad [2B-1]$$

$$\begin{aligned} \overline{x}(z) &= E\{x(z)\} \\ &= \overline{x}(0) + \frac{\overline{\Theta}(0)}{\beta}\cdot\left[\, 1 - \exp(-\beta z)\, \right] \end{aligned} \qquad [2B-2]$$

The mean square angle of travel is,

$$\begin{aligned} \sigma_{\Theta}^{2}(z) &= E\{[\Theta(z)-\overline{\Theta}(z)]^{2}\} \\ &= \sigma_{\Theta}^{2}(0)\cdot\exp(-2\beta z) + \frac{1}{2}\int_{0}^{z} k(z')\cdot\exp(-2\beta(z-z')) \end{aligned}$$

[2B-3]

The angular-lateral covariance is,

$$r_{x\Theta}(z) = E\{[x(z)-\overline{x}(z)]\bullet[\Theta(z)-\overline{\Theta}(z)]$$

$$= r_{x\Theta}(0)\bullet\exp(-\beta z) + \frac{\sigma_{\Theta}^{2}(0)}{\beta}\bullet[\exp(-\beta z)-\exp(-2\beta z)]$$

$$- \frac{1}{2\beta}\int_{0}^{z} k(z')\bullet[\exp(-2\beta(z-z'))-\exp(-\beta(z-z'))]\ dz'$$

[2B-4]

Finally, the mean square lateral position is,

$$\sigma_{x}^{2}(z) = E\{[x(z)-\overline{x}(z)]^{2}\}$$

$$= \sigma_{x}^{2}(0) + \frac{2r_{x\Theta}(0)}{\beta}\bullet[1-\exp(-\beta z)] + \frac{\sigma_{\Theta}^{2}(0)}{\beta^{2}}\bullet[1-\exp(-\beta z)]^{2}$$

$$+ \frac{1}{2\beta^{2}}\int_{0}^{z} k(z')\bullet\exp(-2\beta z)\bullet[\exp(\beta z)-\exp(\beta z')]^{2}\ dz'$$

[2B-5]

To summarize, the parameters specifying the jointly Gaussian probability density predicted by the restricted scattering model are,

$$\overline{\Theta}(z) = \overline{\Theta}(0)\bullet\exp(-\beta z) \qquad [2B\text{-}6a]$$

$$\overline{x}(z) = \overline{x}(0) + \frac{\overline{\Theta}(0)}{\beta}\bullet(1-\exp(-\beta z)) \qquad [2B\text{-}6b]$$

$$\sigma_{\Theta}^{2}(z) = A_{0}(z) + \sigma_{\Theta}^{2}(0)\bullet\exp(-2\beta z) \qquad [2B\text{-}6c]$$

$$r_{x\Theta}(z) = A_{1}(z) + \frac{\sigma_{\Theta}^{2}(0)}{\beta}\bullet\Big[\ \exp(-\beta z)\ -\ \exp(-2\beta z)\ \Big]$$

$$+\ r_{x\Theta}(0)\bullet\exp(-\beta z) \qquad [2B\text{-}6d]$$

$$\sigma_x^2(z) = A_2(z) + \frac{\sigma_\theta^2(0)}{\beta^2} \bullet \left[1 - \exp(-\beta z) \right]^2$$

$$+ \frac{2r_{x\theta}(0)}{\beta} \bullet \left[1 - \exp(-\beta z) \right] + \sigma_x^2(0) \qquad [2B\text{-}6e]$$

The moments, $A_i(z)$ $(i=0,1,2)$, are given by,

$$A_i(z) = \frac{1}{2} \int_0^z k(z') \bullet \left[\frac{\exp(\beta(z-z'))-1}{\beta} \right]^i \exp(-2\beta(z-z'))\, dz'$$

$$[2B\text{-}7]$$

These are the parameters [2-14] given in section 2.2.

Chapter 3

A Numerical Algorithm for Transport Calculations

3.1 Infinitesimal Integral Formula for Small Angles

In this section, we derive an integral which allows the determination of the electron probability density at a depth, $z+\delta$, given the electron probability density at a depth, z. This provides a means to propagate an incident electron probability density through a heterogeneous medium in increments of depth, δ.

The derivation may be done for two lateral dimensions, x and y. In chapter two it was noted that the Fermi-Eyges transport equation is separable and scattering in the xz plane and yz plane may be treated separately. Only scattering in the xz plane is considered here and the beam and inhomogeneities are taken to be infinite in the y direction.

Let us start by noting that the probability density at depth, $z+\delta$, will, in general, be given by

$$F(z+\delta,x,\Theta) = \int_{-\infty}^{\infty} \int_{-\infty}^{\infty} F(z,x',\Theta') \bullet p_{\delta}(x,\Theta;x',\Theta')\, dx' d\Theta' \qquad [3-1]$$

where $F(z,x,\Theta)$ is the electron probability density at depth, z, lateral position, x, and angle Θ. The function, $p_{\delta}(x,\Theta;x',\Theta')$, represents the transition density for an electron to reach (x,Θ) in an increment of depth, δ, given that it starts at coordinates (x',Θ'). In other words, the probability that an electron starts at depth z with position x' and direction Θ' and arrives at depth $z+\delta$ with position in the interval $[x,x+dx]$ and direction in the interval $[\Theta,\Theta+d\Theta]$ is $p_\delta(x,\Theta;x',\Theta')dxd\Theta$. The function, $p_\delta(x,\Theta;x',\Theta')$, may also be referred to as the Green's function or scattering kernel.

The Fermi-Eyges model predicts that the angular transition density is Gaussian (section 2.1). If we assume that the scattering power is constant in the small increment of depth, δ, then the angular transition density is given by,

$$p_\Theta(\Theta;\Theta') = C\bullet\exp\{-(\Theta-\Theta')^2/k\delta\} \qquad [3\text{-}2a]$$

$$\text{where} \qquad C = 1/\sqrt{\pi k\delta} \qquad [3\text{-}2b]$$

The lateral transition density, according to the Fermi-Eyges model, is also Gaussian with a variance, $k\delta^3/6$. This is much less than the variance, $k\delta/2$, for the angular transition density [3-2] provided δ is small. Therefore, the lateral transition density may be approximated by a Dirac delta function

$$p_x(x;x') \approx \delta_{dirac}\{x - (x'+\Theta\delta+\alpha(\Theta'-\Theta)\delta)\} \qquad [3\text{-}3]$$

In other words, electrons starting at (x',Θ') end up with lateral position $x'+\Theta\delta+\alpha(\Theta'-\Theta)\delta$ with probability 1 and their angular distribution is determined by [3-2]. The constant, α, is introduced to allow for the fact that the electrons scatter continuously as they travel from depth, z, to depth, $z+\delta$. If, instead, the electron scattered from angle Θ' to Θ at depth, z, and drifted freely to depth, $z+\delta$, then the change in lateral position becomes simply $\Theta\delta$ (i.e. $\alpha=0$). Conversely, if all the scattering took place at depth, $z+\delta$, then the change in lateral position becomes $\Theta'\delta$ (i.e. $\alpha=1$). We expect that the change in lateral position would be somewhere between these two extremes so that $0\leq\alpha\leq1$. It will be seen, in fact, that α can be chosen arbitrarily as any finite real number.

Neglecting terms of order higher than δ, it is possible to write the complete transition density as a product of [3-2] and [3-3]. The integral [3-1] then becomes

$$F(z+\delta,x,\Theta) = \int_{-\infty}^{\infty} F(z,x-\Theta\delta-\alpha(\Theta'-\Theta)\delta,\Theta')\bullet p(\Theta;\Theta')\ d\Theta' \tag{3-4}$$

where the subscript Θ on the function $p_\Theta(\Theta;\Theta')$ has been dropped for convenience.

Making the change of variables, $\phi=\Theta'-\Theta$, the integral becomes,

$$F(z+\delta,x,\Theta) = \int_{-\infty}^{\infty} F(z,x-(\Theta+\alpha\phi)\delta,\Theta+\phi)\bullet p(\Theta;\Theta+\phi)\ d\phi \qquad [3\text{-}5]$$

With $\alpha=0$, equation [3-5] reduces to the infinitesimal integral formula given by Storchi and Huizenga (1985). With $\alpha=1$, equation [3-5] forms the basis of the numerical algorithm which is presented here. In appendix 3A, it is shown that equation [3-5] is equivalent to the Fermi-Eyges differential transport equation up to terms of order δ regardless of the choice of α.

3.2 Infinitesimal Integral Formula for Large Angles

In this section, we introduce a modification of the infinitesimal integral formula [3-5] presented in the previous section. The modification accounts for the fact that the angle of travel of the electrons does not remain small. In this new infinitesimal integral formula, changes in lateral position, x, are equal to $\tan(\Theta+\alpha\phi)\delta$ rather than $(\Theta+\alpha\phi)\delta$. The modified equation is,

$$F(z+\delta,x,\Theta) = \int_{-\pi/2}^{\pi/2} F(z,x-\tan(\Theta+\alpha\phi)\delta,\Theta+\phi)\bullet p(\Theta;\Theta+\phi)\ d\phi \qquad [3\text{-}6]$$

Notice that the limits of the integration have been changed to include only electrons travelling in the forward direction. Also, it should be noted that a similar equation presented in the literature (Jette, 1988) uses $\alpha\tan(\Theta-\phi)+(1-\alpha)\tan\Theta$ intead of $\tan(\Theta+\alpha\phi)$. The two equations are equivalent in the sense that they both lead to the same differential equation up to terms of order δ regardless of the choice of α.

In appendix 3B, it is shown that, up to terms of order δ, equation [3-6] is equivalent to the differential transport equation,

$$\frac{dF}{dz} = -\tan(\Theta)\,\frac{dF}{dx} + \frac{k}{4}\cdot\frac{d^2F}{d\Theta^2} \qquad [3\text{-}7]$$

Equation [3-6] may be used as the basis of a numerical algorithm which propagates an incident electron probability density through a heterogeneous medium.

3.3 Numerical Implementation of the Infinitesimal Integral Formula

The first step in modifying the infinitesimal integral equation [3-5] or [3-6] for use in a numerical algorithm is to discretize the probability density, $F(z,x,\Theta)$. The probability density will be defined only at a finite number of points, (z_i,x_j,Θ_k), for $i=1,..,N_z$, $j=1,..,N_x$ and $k=-N_\Theta,..,N_\Theta$. The number of depth increments is N_z, the number of lateral increments is N_x and the number of angular increments is $2N_\Theta+1$. Also, the size of the depth, lateral and angular increments will be δ, Δx and $\Delta\Theta$ respectively.

The integrals [3-5] and [3-6] must also be discretized. Assuming that the angular increments are small enough that the probability density does not change much in any given angular interval, $(\Theta_k-\Delta\Theta/2,\Theta_k+\Delta\Theta/2)$, and the probability density is essentially zero beyond some maximum angle $N_\Theta\cdot\Delta\Theta$, then equation [3-5] may be written,

$$F(z+\delta,x,\Theta) \approx \sum_{k=-N_\Theta}^{N_\Theta} F(z,x-\Theta_k\delta,\Theta_k)\cdot\int_{\Theta_k-\Delta\Theta/2}^{\Theta_k+\Delta\Theta/2} p(\Theta;\Theta')\, d\Theta' \qquad [3\text{-}8]$$

A completely analogous discrete version of [3-6] may also be obtained. The integral within the sum represents the probability that an electron scatters from an interval of angle $\Delta\Theta$ centred on Θ_k to an angle Θ. The integral will be denoted by $P(\Theta,\Theta_k,\Delta\Theta)$ and, using [3-2], it may be written as a difference of error functions,

$$P(\Theta,\Theta_k,\Delta\Theta) = ½\,[\mathrm{erf}\{(\Theta-\Theta_k+\Delta\Theta/2)/\sqrt{k\delta}\,\} - \mathrm{erf}\{(\Theta-\Theta_k-\Delta\Theta/2)/\sqrt{k\delta}\,\}] \qquad [3\text{-}9]$$

where erf denotes the error function (Arfken,1970). The scattering power, k, will vary with both electron energy and the type of scattering material and may be different at different points in a heterogeneous medium. In other words, $k=k(E,x,y,z)$. (note: although k is used for both scattering power and the angular index, the meaning will be clear from the context).

The problem with direct implementation of [3-8] is the fact that the lateral points, $x-\Theta_k\delta$, do not necessarily coincide with the discrete lateral points, x_j. The sum is, therefore, built up in an indirect way. Electrons at a point (z_i,x_j,Θ_k) are translated to a point $(z_{i+1},x_j+\Theta_k\delta,\Theta_k)$ and, using a linear interpolation, electrons are shared between the two discrete lateral points nearest to $x_j+\Theta_k\delta$. Using equation [3-9], electrons are then spread into angular points around Θ_k. This procedure is repeated for each of the discrete points in the plane corresponding to depth z_i. The process is shown schematically in figure 3.1 and each step is described in detail in table 3.1.

The steps described in table 3.1 form the core of the numerical algorithm since they allow the discrete probability density at depth, $z+\delta$, to be determined from the probability density at depth, z. As long as the probability density is known at the surface of a medium, the process may be applied to each plane in succession in order to build up the complete probability density. Methods of calculating the electron distribution from a clinical electron linear accelerator at the surface of a medium have been described in the literature for magnetically scanned beams (Huizenga

Figure 3.1

Schematic diagram for the propagation of electrons in the numerical algorithm.

The propagation of electrons from a point at depth, z_i, into points at depth, z_{i+1}, is shown schematically. Electrons are first projected into the z_{i+1} plane. They are then shared between the two closest discrete lateral points and finally they are spread into angular points. The process is described in detail in table 3.1.

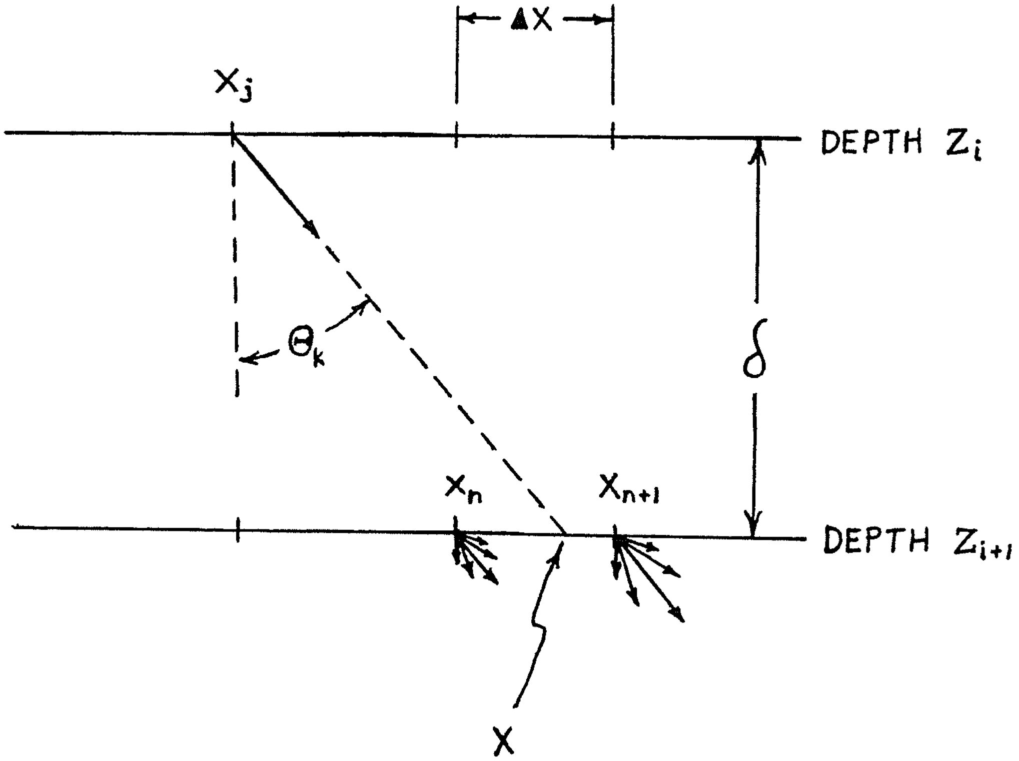
ΔX
X_j
DEPTH Z_i
Θ_k
δ
X_n
X_{n+1}
DEPTH Z_{i+1}
X

Table 3.1 Logic flow for a numerical method of electron transport calculations.

Step	Description
1	Choose a point z_i, x_j, Θ_k.
2	Project to a lateral point in the z_{i+1} plane: $x = x_j + \Theta_k \delta$ for small angles and $x = x_j + \tan(\Theta_k)\delta$ for large angles
3	Find the discrete points, x_n and x_{n+1}, which are closest to x.
4	Calculate the weighting functions for the linear interpolation: $W_A = \lvert x_n - x \rvert / \blacktriangle x$ and $W_B = \lvert x_{n+1} - x \rvert / \blacktriangle x$
5	For each discrete angular point, Θ_m, $(m = -N_\Theta, \ldots, N_\Theta)$ assign probability densities to the points (z_{i+1}, x_n, Θ_m) and $(z_{i+1}, x_{n+1}, \Theta_m)$ according to the rules*, $F(z_{i+1}, x_n, \Theta_m) = F(z_{i+1}, x_n, \Theta_m) + W_B \bullet F(z_i, x_j, \Theta_k) \bullet P(\Theta_m, \Theta_k, \blacktriangle\Theta)$ $F(z_{i+1}, x_{n+1}, \Theta_m) = F(z_{i+1}, x_{n+1}, \Theta_m) + W_A \bullet F(z_i, x_j, \Theta_k) \bullet P(\Theta_m, \Theta_k, \blacktriangle\Theta)$
6	Repeat steps 1 through 5 for each point in the z_ith plane.

* The sign "=" is to be read " assigned the value of". The function, $P(\Theta_m, \Theta_k, \blacktriangle\Theta)$, is given by equation [3-9].

and Storchi,1987; Sandison and Huda,1988).

3.4 Incorporation of Electron Energy Loss in the Algorithm

The energy loss of the electrons must be included in order to calculate realistic distributions. In the present algorithm, an energy is associated with each lateral point and it is assumed that the energy of the electrons is independent of the angle of travel. The energy at a given lateral point is calculated from,

$$E(z+\delta, x_j) = E(z, x_j) - S_{tot}\bullet\delta \qquad [3\text{-}10]$$

where $E(z,x)$ indicates the kinetic energy of an electron at point (z,x) and S_{tot} is the total stopping power for electrons of the appropriate energy in the given material. Therefore, the electron energy at a point is dependent only upon the energy and type of material associated with the point immediately above.

The stopping power in water for any electron energy may be obtained by a fit to published data (ICRU,1984). In this case, the stopping power data has been fitted to the formula,

$$S_{tot}^{w}(E) = a + bE + \frac{c}{E} \qquad [3\text{-}11]$$

where the superscript, w, indicates that the medium is water. Using a least squares fit, the constants are found to be a=1.792 MeV/cm, b=0.03212 cm^{-1} and c=0.08497 MeV^2/cm. The least squares fit is compared with published data in figure 3.2. Over the range 0.5 to 35 MeV, the fit is within 3% of the true value.

A means of obtaining the stopping power in media other than water is now required. Huizenga and Storchi (1985) suggest that, for materials and electron energies of clinical interest, the stopping power may be scaled according to the relative electron density of the medium (the electron density of the medium divided by the electron density of water). Therefore, provided the relative electron density is known throughout a heterogeneous medium, the electron energy may be calculated at all points given an incident beam energy.

3.5 Requirements for Grid Spacing

The use of a discrete calculation grid is only an approximation to the continuous case. The required size of the grid increments to achieve sufficient accuracy must be known and in this section the limits for the coarseness of the calculation grid are discussed.

As discussed in sections 3.1 and 3.2, the infinitesimal integral formulas are accurate up to order δ (the size of

Figure 3.2

Stopping power for electrons in water as a function of energy.

Stopping power for electrons in water is shown as a function of the electron kinetic energy. The solid line represents the "true" values taken from ICRU report 37 (ICRU,1984). The dashed line is a fit to the equation,

$$S_{tot}^{w} = a + bE + c/E$$

Using a least squares fit, the constants a,b and c are found to be,

$a = 1.792$ MeV/cm

$b = 0.03212$ cm^{-1}

$c = 0.08497$ MeV^{2}/cm

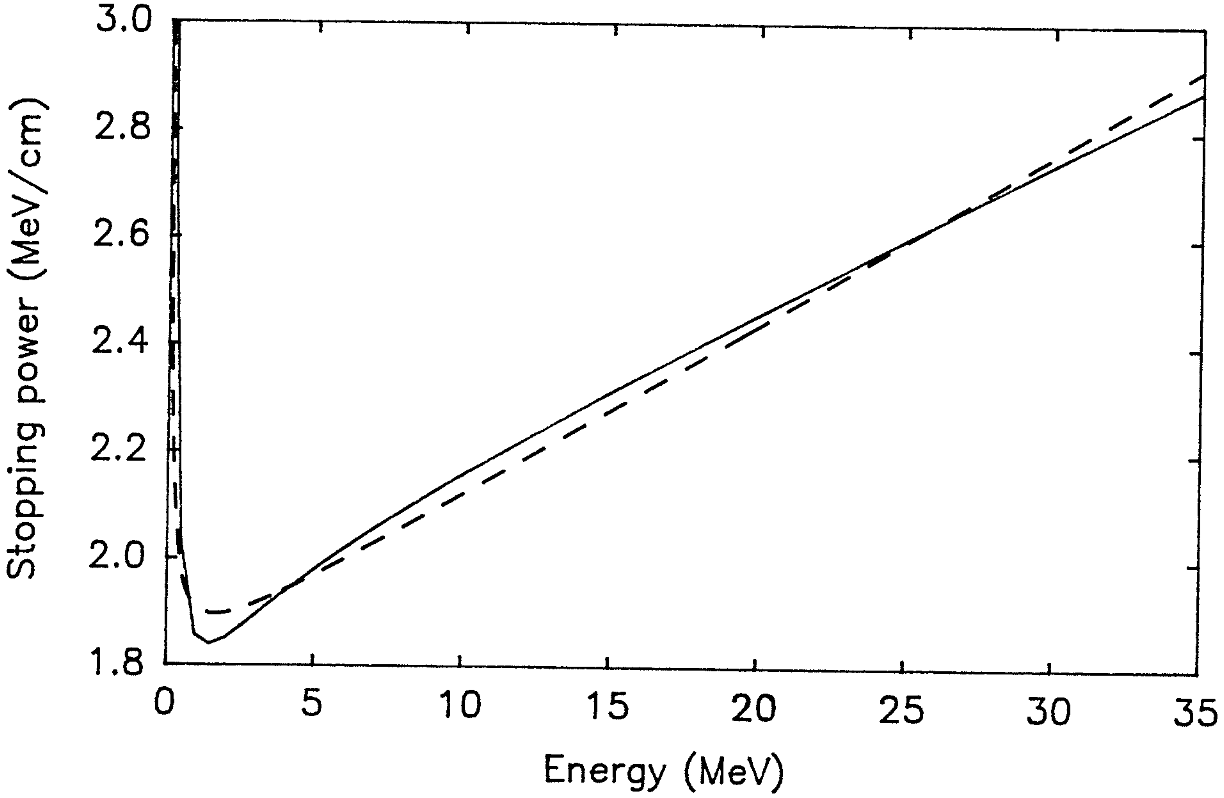
3.0
2.8
2.6
2.4
2.2
2.0
1.8
Stopping power (MeV/cm)
0
5
10
15
20
25
30
35
Energy (MeV)

the depth increments). Therefore, the depth increments should be made as small as possible, allowing for limitations in calculation time and computer memory.

Recall that the angular transition density is Gaussian with variance $k\delta/2$. To predict the angular spreading of electrons accurately, the angular grid increment should be small compared to the root mean square spread in the angular transition density,

$$\Delta\Theta \ll (k\delta/2)^{1/2} \qquad [3\text{-}12]$$

A basic assumption of both the infinitesimal integral equations [3-5] and [3-6] is that the spread of the lateral transition density is negligible (i.e. it is approximated by a Dirac delta function). Therefore, it would not be correct to impose a condition analogous to [3-12] on the lateral grid increments. Instead, we require that,

$$\frac{dF(z,x,\Theta)}{dx} \cdot \Delta x \ll 1 \qquad [3\text{-}13]$$

In other words, the change in the probability density in a distance, Δx, must be small. The lateral variation of the probability density can be very rapid for a narrow beam and this represents a severe test of the algorithm. Near the surface of the scattering medium, a pencil beam will always be in violation of the condition [3-13]. However, as the electrons penetrate the scattering medium, they will spread laterally so that the beam is better approximated by a discrete grid. It is shown in section 3.6 that the performance of the algorithm for an incident pencil beam is satisfactory.

Broad clinical beams vary much more slowly in the lateral direction than narrow beams and it is expected that they will be better approximated by a discrete lateral grid. In the case of calculations with clinical beams, the lateral increment size is normally chosen to be about 2 or 3 mm.

Note that the angular grid spacing is determined by the angular scattering power, k, and the depth increment, δ (see [3-12]). In practice, the number of angular and lateral increments is limited by the available computer memory. Given a scattering power (i.e. an incident beam energy and type of scattering medium) the depth increment, δ, may be chosen to satisfy both [3-12] and the computer memory requirements.

3.6 Calculations in Homogeneous Media: Small Angles

It is the aim of this section to compare the results of calculations using the numerical algorithm to the theoretical predictions of the Fermi-Eyges model. The purpose of such a comparison is to show that the algorithm is successful in reproducing known results. These calculations have been performed for both pencil beams and broad beams using the numerical algorithm based on the "small angle" equation [3-5].

There are several algorithm parameters which may be varied. These are the number of angular bins, $2N_\Theta+1$, the number of lateral bins, N_x, the number of depth increments, N_z, the angular increment size, $\Delta\Theta$, the lateral increment size, Δx, and the size of the depth increments, δ. Due to the limited memory available (64K) on the DEC LSI 11/73 computer on which the calculations were performed, N_Θ and N_x were set to 30 and 64 respectively for all runs. Since the number of angular increments is set, the choice of the angular increment size determines the maximum grid angle.

The first set of calculations was designed to test the effects of varying the lateral grid spacing, Δx, and the size of the angular increments, $\Delta\Theta$. For a point monodirectional pencil beam incident on water, three calculations were performed for Δx equal to 0.3 cm, 0.2 cm and 0.15 cm. For all three calculations, N_z, δ and $\Delta\Theta$ were set to 20, 0.3 cm and 0.051501 radians respectively. Note that the angular increment size corresponds to a maximum grid angle of $\pi/2$ radians.

The mean square angle of travel produced by these calculations is plotted as a function of depth in figure 3.3. For comparison, the Fermi-Eyges prediction is also

Figure 3.3

Mean square angle of travel versus depth - theoretical calculations and numerical algorithm results.

The mean square angle of travel is shown as a function of depth for a 10 MeV point monodirectional pencil beam incident on water. The symbols represent the numerical algorithm results and the solid line represents the Fermi-Eyges prediction. The parameters used in the numerical algorithm are:

$N_\Theta = 30$

$N_x = 64$

$N_z = 20$

$\Delta\Theta = 0.051501$ rad

$\Delta x = 0.3$ cm, 0.2 cm, 0.15 cm

$\delta = 0.3$ cm

Note that all three lateral grid spacings produce exactly the same mean square angular spread. Also, the angular increments, $\Delta\Theta$, are chosen to correspond to a maximum grid angle of $\pi/2$ radians.

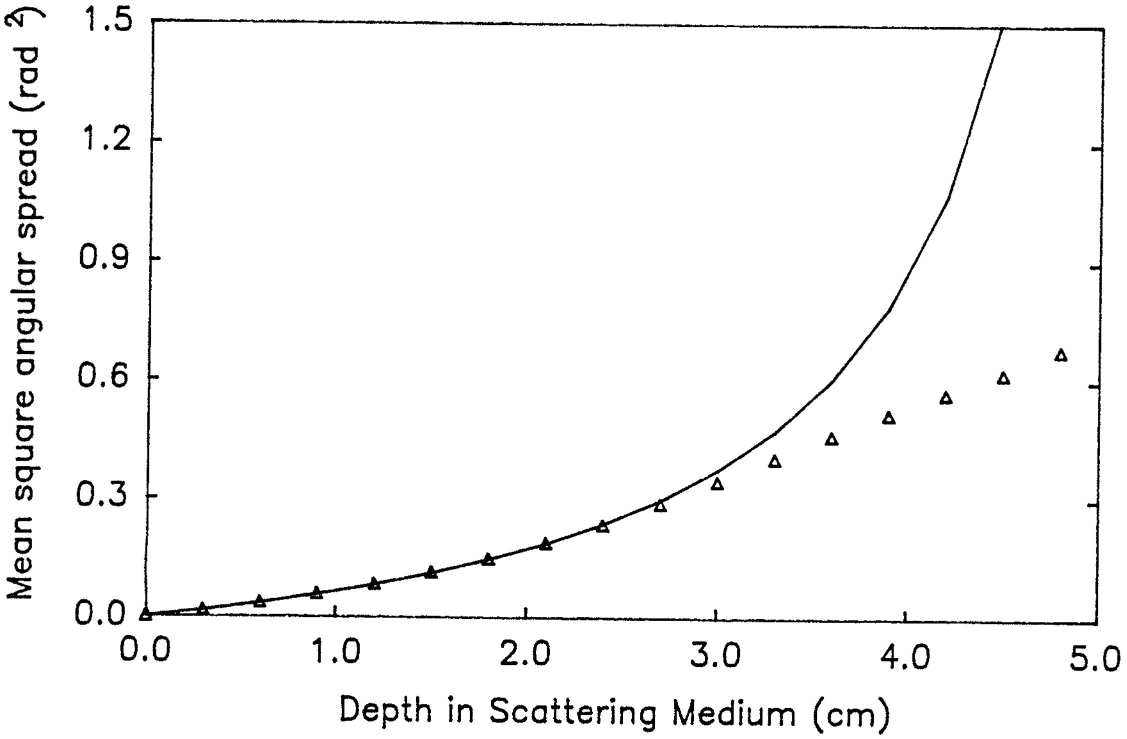
Mean square angular spread (rad 2)
1.5
1.2
0.9
0.6
0.3
0.0
0.0
1.0
2.0
3.0
4.0
5.0
Depth in Scattering Medium (cm)

Figure 3.4

Mean square lateral position versus depth - theoretical
calculations and numerical algorithm results.

The mean square lateral position is shown as a function of depth for a 10 MeV monodirectional pencil beam incident on water. The numerical algorithm parameters are the same as in figure 3.3. The symbols correspond to three different lateral grid spacings: ▲x=0.3 cm (triangles), ▲x=0.2 cm (squares) and ▲x=0.15 cm (inverted triangles). As in figure 3.3, the maximum grid angle is $\pi/2$ radians.

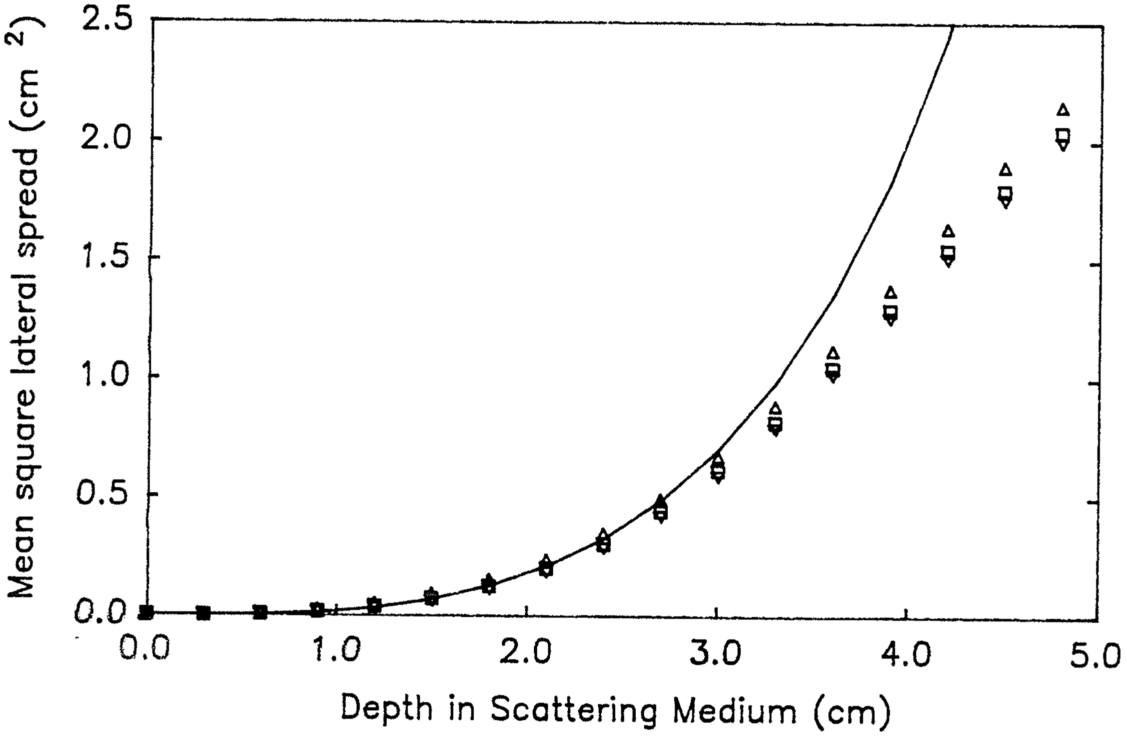
Mean square lateral spread (cm ^{2})
2.5
2.0
1.5
1.0
0.5
0.0
0.0
1.0
2.0
3.0
4.0
5.0
Depth in Scattering Medium (cm)

plotted. The mean square lateral position is plotted in figure 3.4 for the same calculations.

It is evident from figures 3.3 and 3.4 that the agreement between the algorithm calculations and theoretical predictions is excellent at shallow depths but becomes poor deep in the scattering medium. The reason for the discrepancy is the fact that many electrons attain an angle greater than $\pi/2$ deep in the medium and are lost from the calculation grid. The result is an under estimation of the mean square angle of travel and mean square lateral position.

To demonstrate that this is the case, the calculations were re-done using the same parameters except for a change in ▲Θ. The size of the angular increments, ▲Θ, was increased to correspond to a maximum grid angle of π radians. Figures 3.5 and 3.6 show the mean square angle of travel and mean square lateral position respectively for this second set of calculations. As expected, the agreement between the algorithm results and theoretical predictions is much better.

Figures 3.7, 3.8 and 3.9 show the pencil beam profiles at 1.5 cm, 3.0 cm and 4.5 cm depth respectively for the same beam and grid parameters as in figures 3.5 and 3.6. It may be seen that the agreement between the theoretical predictions and algorithm results improves as the lateral grid spacing is made smaller. Also, the least favourable

Figure 3.5

Mean square angle of travel versus depth - theoretical calculations and numerical algorithm results.

The mean square angle of travel is shown as a function of depth for a 10 MeV point monodirectional pencil beam incident on water. The symbols represent the numerical algorithm results and the solid line represents the Fermi-Eyges prediction. The parameters used in the numerical algorithm are:

$N_\Theta = 30$

$N_x = 64$

$N_z = 20$

$\Delta\Theta = 0.10300$ rad

$\Delta x = 0.3$ cm, 0.2 cm, 0.15 cm

$\delta = 0.3$ cm

Note that all three lateral grid spacings produce exactly the same mean square angular spread. Also, the maximum grid angle is π radians. There is a marked improvement over the case where the maximum grid angle is $\pi/2$ (figure 3.3).

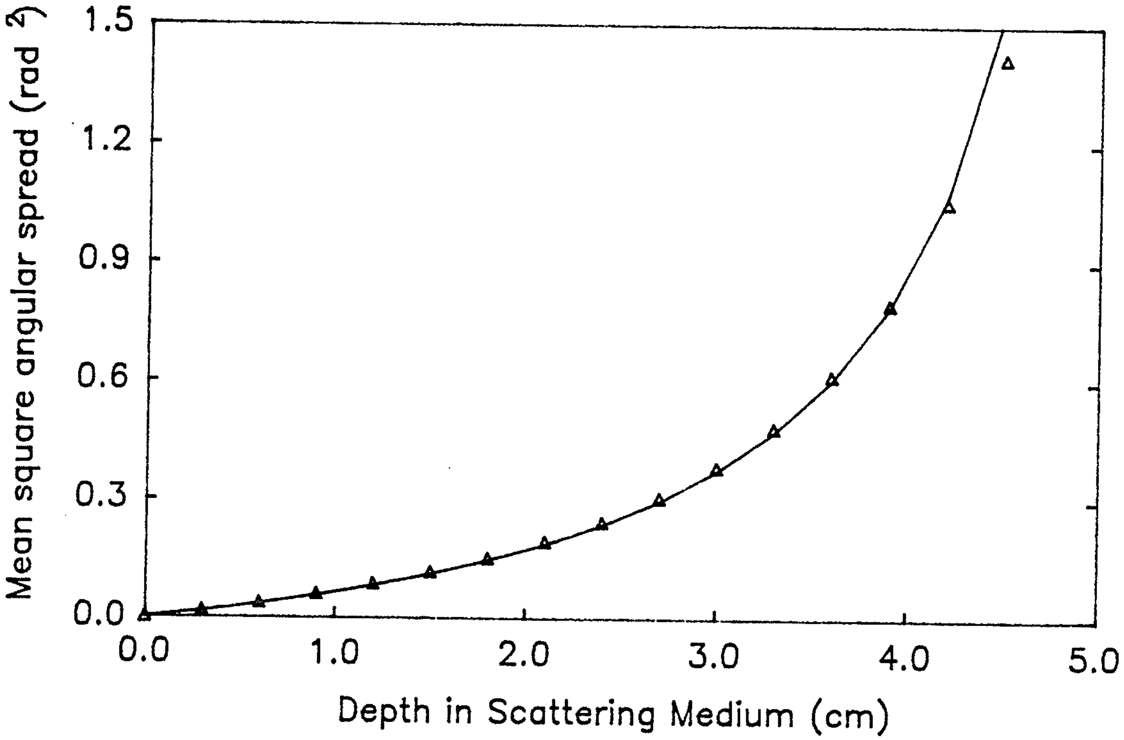
Mean square angular spread (rad 2)
1.5
1.2
0.9
0.6
0.3
0.0
0.0
1.0
2.0
3.0
4.0
5.0
Depth in Scattering Medium (cm)

Figure 3.6

Mean square lateral position versus depth - theoretical calculations and numerical algorithm results.

The mean square lateral position is shown as a function of depth for a 10 MeV monodirectional pencil beam incident on water. The numerical algorithm parameters are the same as in figure 3.5. The symbols correspond to three different lateral grid spacings: ▲x=0.3 cm (triangles), ▲x=0.2 cm (squares) and ▲x=0.15 cm (inverted triangles). As in figure 3.5, the maximum grid angle is π radians. Note the significant improvement over the case where the maximum grid angle is π/2 (figure 3.4).

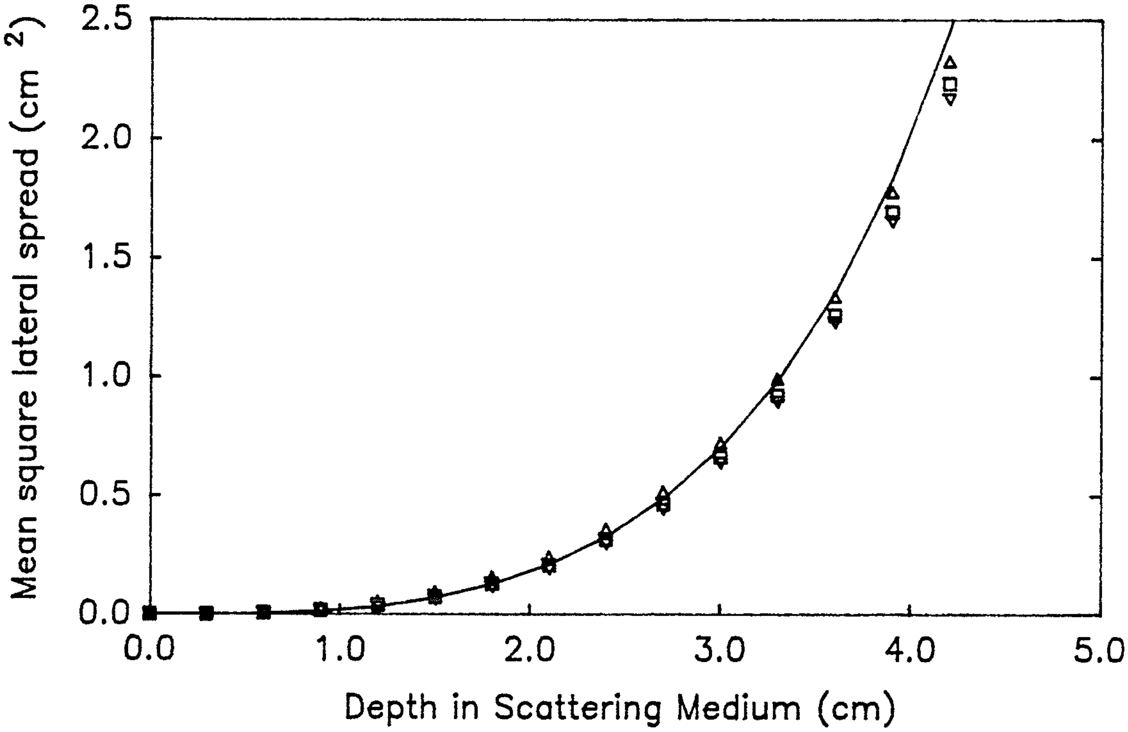

Mean square lateral spread (cm ^{2})
2.5
2.0
1.5
1.0
0.5
0.0
0.0
1.0
2.0
3.0
4.0
5.0
Depth in Scattering Medium (cm)

Figure 3.7

Beam profile at 1.5 cm depth in water for an incident 10 MeV point monodirectional pencil beam.

The electron fluence as predicted by the Fermi-Eyges model and as calculated by the numerical algorithm at 1.5 cm depth is shown for a 10 MeV pencil beam incident on water. Each fluence profile has been normalized to 100% on the central axis. Only half the profile is shown since it is symmetric about x=0. The solid line is the Fermi-Eyges prediction and the symbols represent the numerical algorithm results for $\Delta x=0.3$ cm (triangles), $\Delta x=0.2$ cm (squares) and $\Delta x=0.15$ cm (inverted triangles). The remaining algorithm parameters are:

$N_\theta = 30$

$N_x = 64$

$N_z = 20$

$\Delta\Theta = 0.10300$ rad

$\delta = 0.3$ cm

These parameters are the same as in figure 3.5.

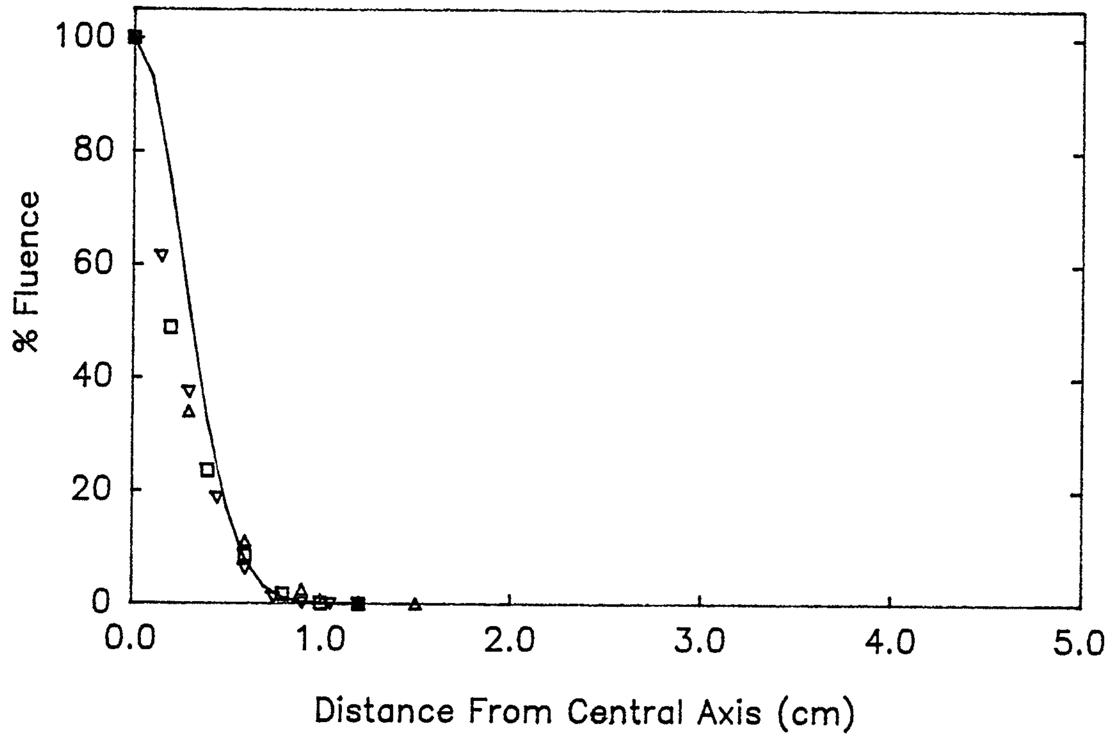

100
80
60
40
20
0
% Fluence
0.0
1.0
2.0
3.0
4.0
5.0
Distance From Central Axis (cm)

Figure 3.8

Beam profile at 3.0 cm depth in water for an incident 10 MeV point monodirectional pencil beam.

The electron fluence as predicted by the Fermi-Eyges model and as calculated by the numerical algorithm at 3.0 cm depth is shown for a 10 MeV pencil beam incident on water. Each fluence profile has been normalized to 100% on the central axis. Only half the profile is shown since it is symmetric about x=0. The solid line is the Fermi-Eyges prediction and the symbols represent the numerical algorithm results for ▲x=0.3 cm (triangles), ▲x=0.2 cm (squares) and ▲x=0.15 cm (inverted triangles). The remaining algorithm parameters are identical to those of figure 3.7. Note that the agreement between the algorithm results and the theoretical prediction improves as ▲x becomes smaller.

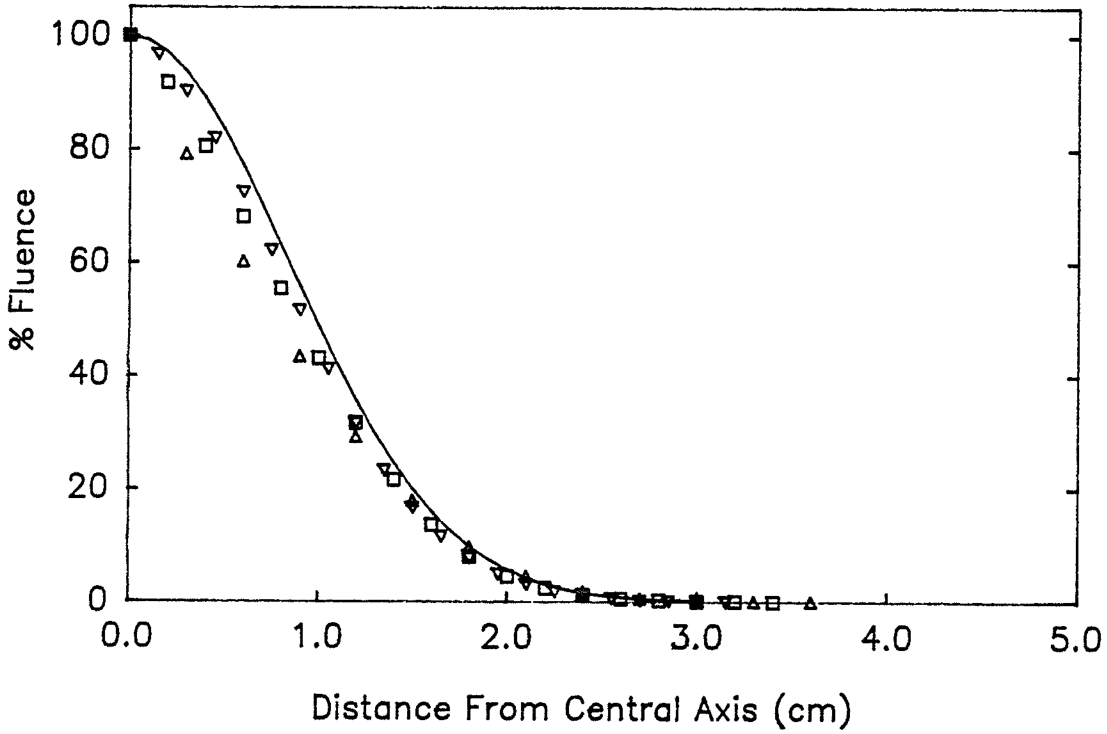
100
80
60
40
20
0
% Fluence
0.0
1.0
2.0
3.0
4.0
5.0
Distance From Central Axis (cm)

Figure 3.9

Beam profile at 4.5 cm depth in water for an incident 10 MeV point monodirectional pencil beam.

The electron fluence as predicted by the Fermi-Eyges model and as calculated by the numerical algorithm at 4.5 cm depth is shown for a 10 MeV pencil beam incident on water. Each fluence profile has been normalized to 100% on the central axis. Only half the profile is shown since it is symmetric about $x=0$. The solid line is the Fermi-Eyges prediction and the symbols represent the numerical algorithm results for $\Delta x=0.3$ cm (triangles), $\Delta x=0.2$ cm (squares) and $\Delta x=0.15$ cm (inverted triangles). The remaining algorithm parameters are identical to those of figure 3.7. Note that the agreement between the algorithm results and the theoretical prediction improves slightly as Δx becomes smaller but all lateral grid spacings produce reasonable agreement with theoretical predictions. This can be contrasted with figures 3.7 and 3.8 where the beam profile varies much more rapidly.

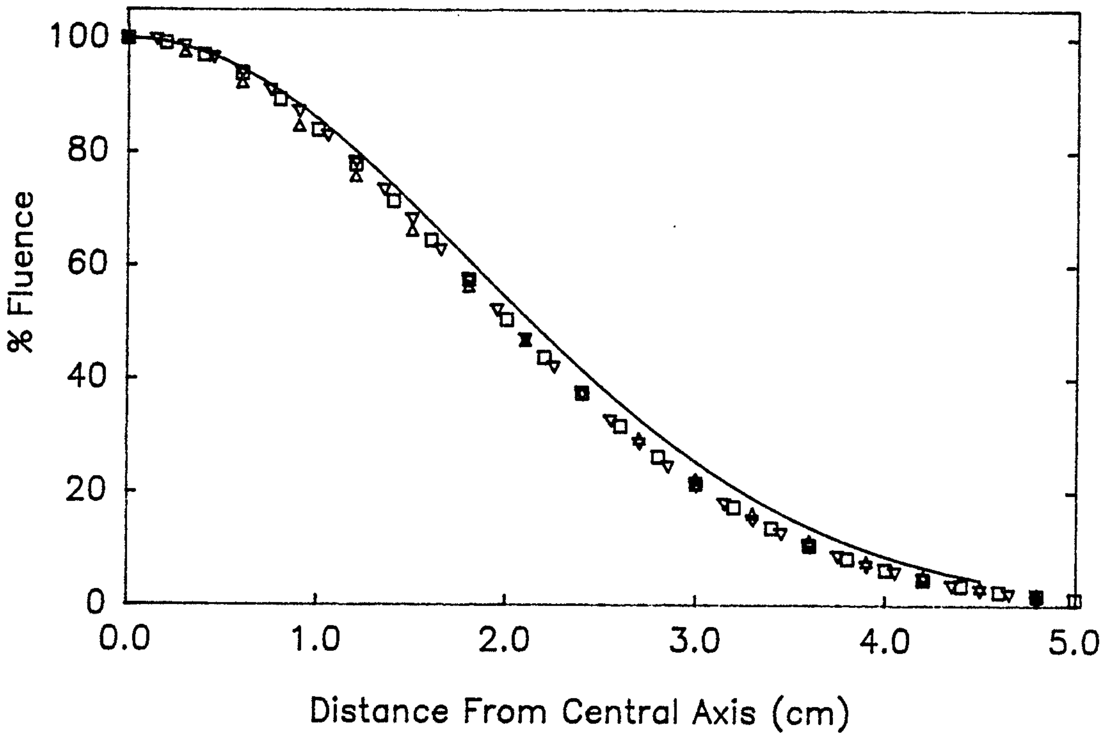
% Fluence
100
80
60
40
20
0
0.0
1.0
2.0
3.0
4.0
5.0
Distance From Central Axis (cm)

results are obtained at shallow depths where the beam profile has the highest dose gradients.

The simulation of a pencil beam is a severe test of the algorithm due to the rapidly varying beam profile. A realistic beam will have a finite lateral and angular spread at the surface of the scattering medium and is more suited to a discrete representation. Calculations have been made for a 10 MeV broad beam incident on water. The angular-lateral electron density at the surface of the water was calculated using the method of Sandison and Huda (1988) assuming a 10x10 cm^2 beam at 100 cm SSD (source-to-surface distance). It was assumed that beam trimmers were in place. The lateral grid increment, Δx, was 0.3 cm and the maximum grid angle was π radians. All other grid parameters were identical to those used in the calculations described above. Beam profiles are shown in figures 3.10, 3.11 and 3.12 for depths of 1.5 cm, 3.0 cm, and 4.5 cm respectively.

3.7 Calculations in Homogeneous Media: Large Angles

This section will compare calculations made using the large angle infinitesimal integral equation [3-6] with calculations made using the analogous small angle equation [3-5]. Also, calculated pencil beam profiles are compared to data presented by Lax et al.(1983).

Lax et al. (1983) have made fits to pencil beam profiles

Figure 3.10

Broad beam profile at 1.5 cm depth for a 10 MeV beam in water.

The electron fluence as predicted by the Fermi-Eyges model and as calculated by the numerical algorithm at 1.5 cm depth is shown for a 10 MeV broad beam in water. The beam is 10x10 cm^2 at 100 cm SSD and trimmers are used. Each of the fluence profiles has been normalized to 100% on the central axis. The solid line is the Fermi-Eyges prediction and the symbols are the algorithm results for the following grid parameters:

$N_\theta = 30$

$N_x = 64$

$N_z = 20$

$\Delta\theta = 0.10300$ rad

$\Delta x = 0.3$ cm

$\delta = 0.3$ cm

The lateral distance between the theoretical prediction and the algorithm results is within one lateral grid increment, Δx, at all points.

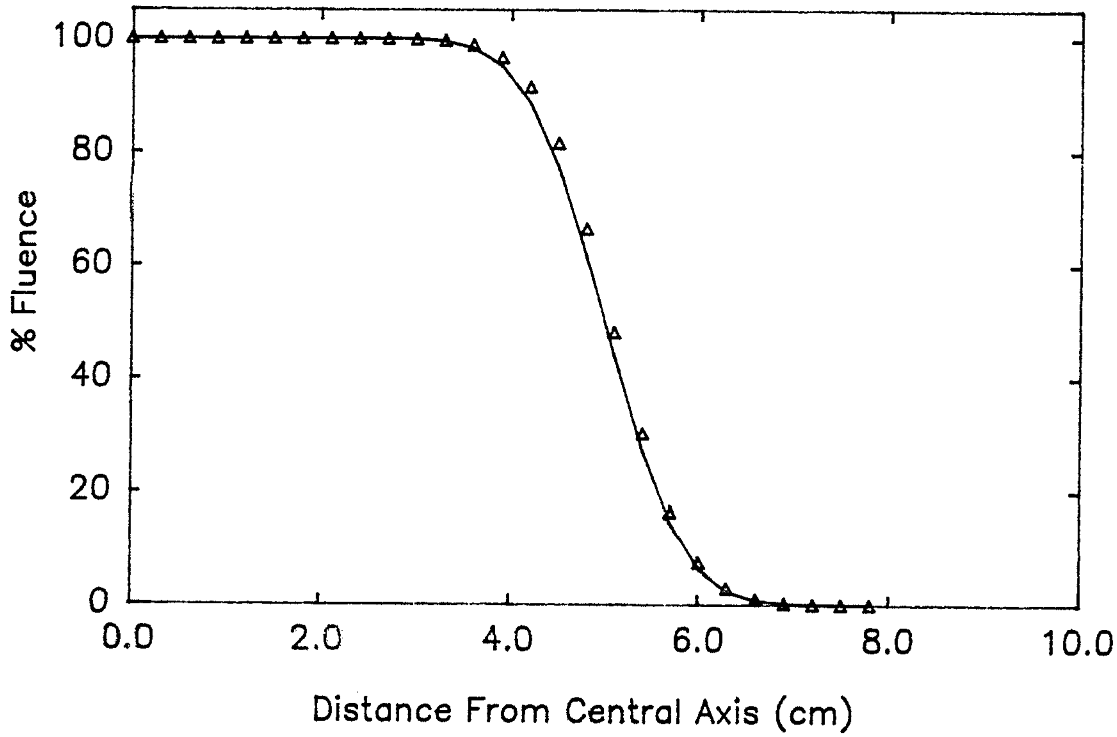
% Fluence
0
20
40
60
80
100
0.0
2.0
4.0
6.0
8.0
10.0
Distance From Central Axis (cm)

Figure 3.11

Broad beam profile at 3.0 cm depth for a 10 MeV beam in water.

The same beam as in figure 3.10 is shown at 3.0 cm depth. Again, the lateral distance between the theoretical prediction and the algorithm results is within one lateral grid increment at all points.

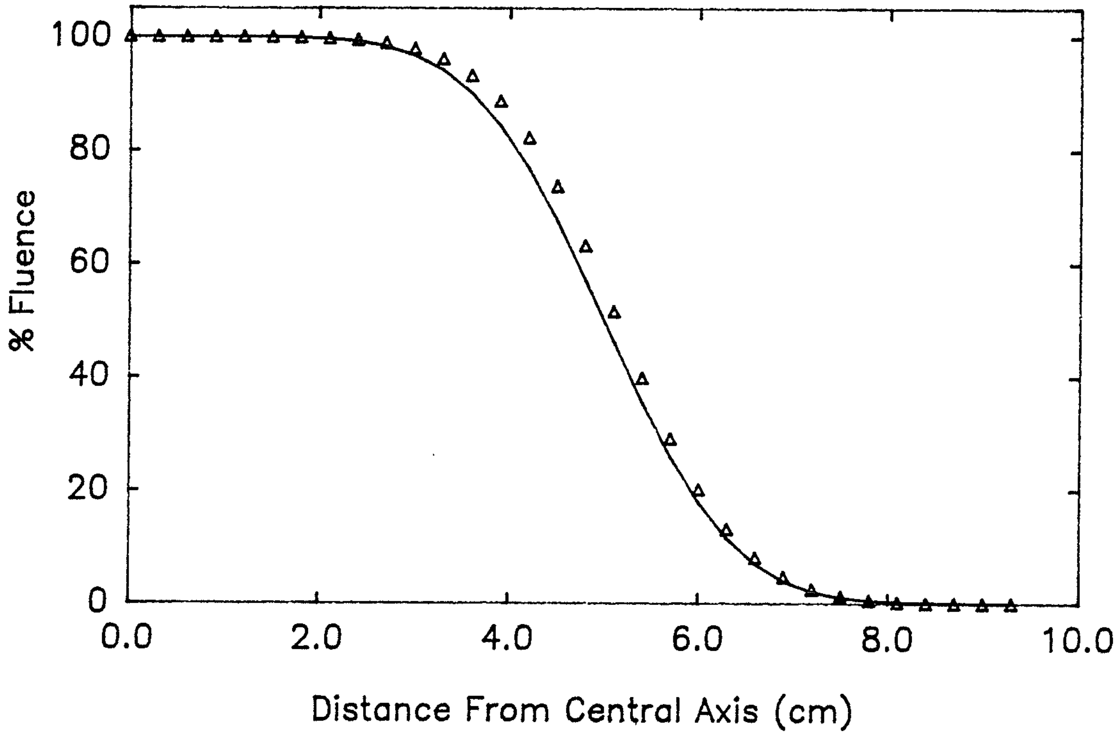
100
80
60
40
20
0
% Fluence
0.0
2.0
4.0
6.0
8.0
10.0
Distance From Central Axis (cm)

Figure 3.12

Broad beam profile at 4.5 cm depth for a 10 MeV beam in water.

The same beam as in figure 3.10 is shown at 4.5 cm depth. Again, the lateral distance between the theoretical prediction and the algorithm results is within one lateral grid increment at all points.

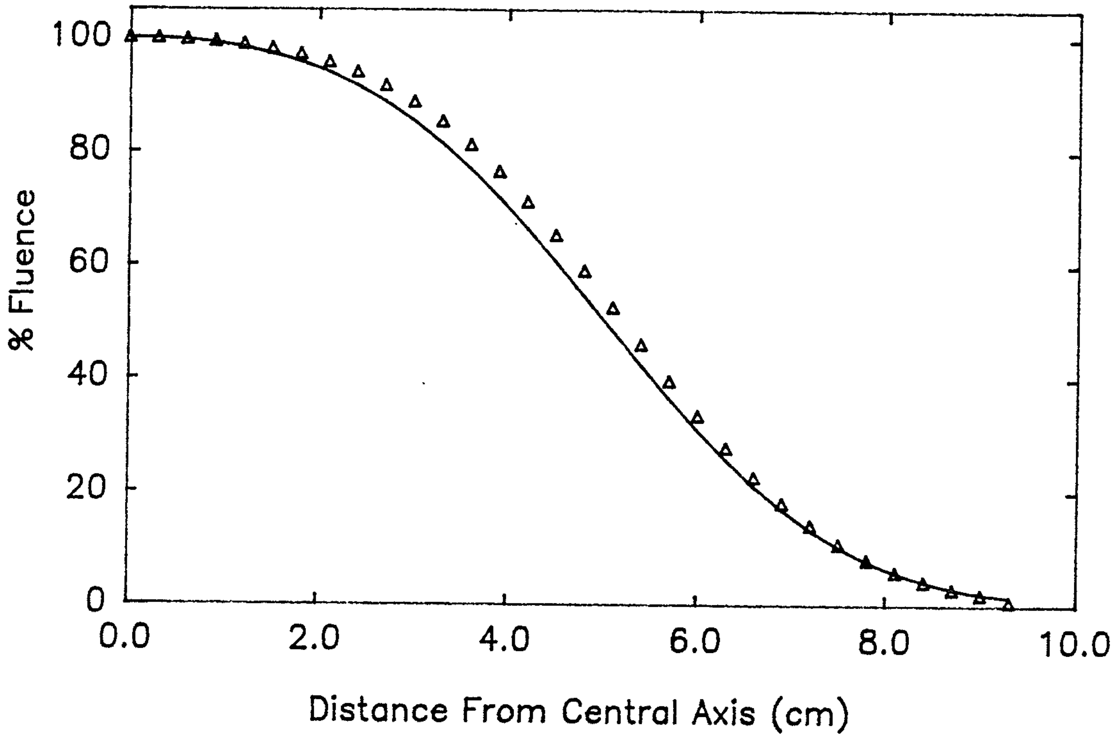
% Fluence
100
80
60
40
20
0
0.0
2.0
4.0
6.0
8.0
10.0
Distance From Central Axis (cm)

calculated using Monte Carlo techniques. The fitted equations are of the form,

$$d(x) = A \cdot \exp(-x^2/a^2) + B \cdot \exp(-x^2/b^2) + C \cdot \exp(-x^2/c^2) \qquad [3\text{-}14]$$

where d(x) is the radial dose profile and x is the lateral distance from the beam axis. The parameters A,B,C,a,b, and c are given in tabular form for several depths at beam energies of 5, 10 and 20 MeV in water. The authors state that the fits are generally within a few tenths of a percent of their Monte Carlo results and deviate by no more than two percent.

As in the previous section, N_Θ and N_x were set to 30 and 64, respectively, due to limitations in the available computer memory. Figures 3.13 and 3.14 show small and large angle calculations compared to the fitted data of Lax et al. (1983) at 2.1 cm and 3.0 cm depth in water for an incident 10 MeV point monodirectional pencil beam. The depth increment, δ, lateral increment, Δx, and angular increment, $\Delta\Theta$, were 0.3 cm, 0.15 cm and 0.051501 radians respectively. Note that the angular increment size corresponds to a maximum grid angle of $\pi/2$ radians.

Figure 3.13

Comparison pencil beam profiles for small and large angle calculations.

Profiles at 2.1 cm depth in water are shown for an incident 10 MeV point monodirectional pencil beam. Calculations were made using the small angle transport equation [3-5] (triangles) and using the large angle transport equation [3-6] (squares). The solid line is the fit to Monte Carlo data given by Lax et al. (1983). It has been assumed that the electron fluence calculated by the algorithm is proportional to dose. All profiles have been normalized to 100% on the central axis.

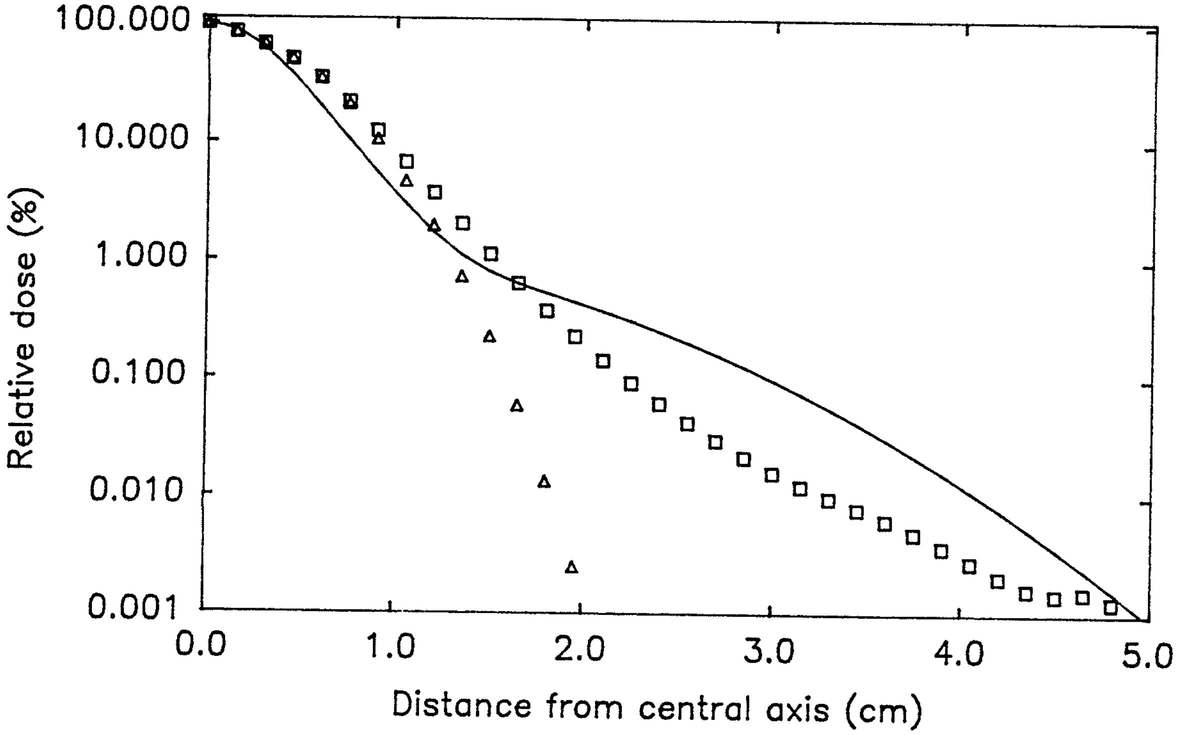
100.000
10.000
1.000
0.100
0.010
0.001
Relative dose (%)
0.0
1.0
2.0
3.0
4.0
5.0
Distance from central axis (cm)

Figure 3.14

Comparison pencil beam profiles for small and large angle calculations.

Profiles at 3.0 cm depth in water are shown for an incident 10 MeV point monodirectional pencil beam. Calculations were made using the small angle transport equation [3-5] (triangles) and using the large angle transport equation [3-6] (squares). The solid line is the fit to Monte Carlo data given by Lax et al. (1983). It has been assumed that the electron fluence calculated by the algorithm is proportional to dose. All profiles have been normalized to 100% on the central axis.

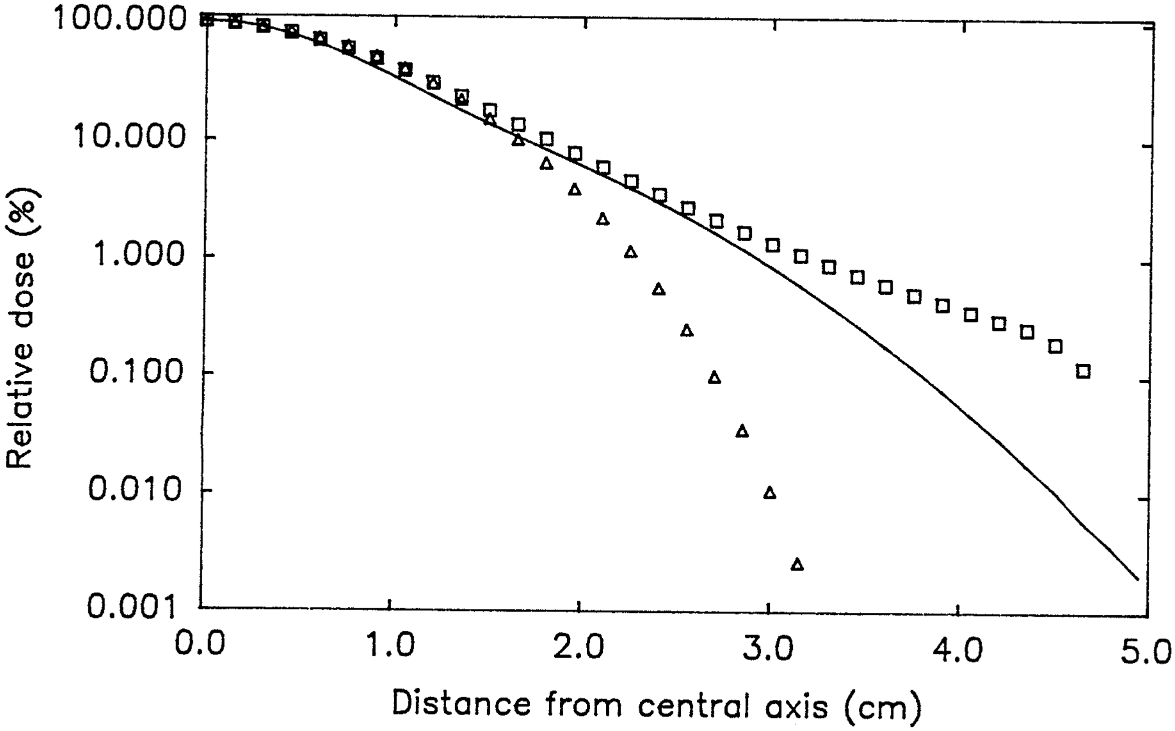

100.000
10.000
1.000
0.100
0.010
0.001
Relative dose (%)
0.0
1.0
2.0
3.0
4.0
5.0
Distance from central axis (cm)

3.8 Discussion

The results of section 3.6 indicate that the algorithm is successful in reproducing known results. Although pencil beam profiles at shallow depths are not well represented by the discrete lateral grid (see figure 3.7), good agreement with analytical results is obtained deeper in the medium (see figures 3.8 and 3.9). Even at shallow depths, however, the lateral distance between the algorithm-generated results and the analytically calculated curve is less than the lateral grid increment, Δx.

In the case of broad beams, the electron probability density varies much more slowly in the lateral direction than it does for a pencil beam. As a result, good agreement is obtained between analytical and algorithm-generated results over the entire electron range. Figures 3.10, 3.11 and 3.12 indicate that the discrepancy is less than the lateral increment size, Δx. It should be noted that this agreement is achieved with the coarsest lateral grid increment (Δx=0.3 cm) that was used in the pencil beam calculations.

Beam energies which are greater than 10 MeV and scattering media which are less dense than water require a smaller angular increment size and/or a larger depth increment size (see [3-12]) than was used in the results presented in sections 3.6 and 3.7. For instance, if the beam energy is doubled, then, for a given angular increment size, $\Delta\Theta$, the depth increment, δ, must be increased by a factor of four (since scattering power, k, varies as the inverse square of the beam energy). For the calculations presented in sections 3.6 and 3.7, the depth increment was 0.3 cm. Therefore, a doubling of the energy would imply a depth increment size of more than a centimeter. A decrease in the angular increment size accompanied by an increase in the number of angular increments would not be possible due to the limitations in the available computer memory.

Figures 3.13 and 3.14 show that the large angle transport equation [3-6] is successful in qualitatively reproducing the broad "tails" in the pencil beam profiles given by Lax et al. (1983). The fitted profiles given by Lax et al. (1983) are based on Monte Carlo calculations which include all types of electron interactions (i.e. bremsstrahlung emission, delta ray production, large angle collisions and small angle multiple scattering are all modeled). The model presented here accounts for only small angle multiple scattering and the lack of quantitative agreement in figures 3.13 and 3.14 is, therefore, not surprising.

A logarithmic scale is used in figures 3.13 and 3.14 to clearly demonstrate the effects of the large angle transport equation [3-6] as compared to the small angle transport equation [3-5]. It should be noted, however, that the differences are large only at points where the dose is less than a few percent of the central axis dose.

3.9 Conclusions

The numerical algorithm presented in this chapter is successful in reproducing known analytical results. For incident electron energies of 10 MeV or less and scattering media with relative electron densities greater than or equal to unity, the agreement with analytically calculated pencil beam and broad beam profiles is within the lateral grid increment, ▲x, at all points. The algorithm based on the large angle transport equation [3-6] predicts, qualitatively, the large angle scattering "tails" in the pencil beam profiles calculated by Monte Carlo techniques (Lax et al., 1983).

Appendix 3A

In this appendix, it is shown that the integral [3-5] is equivalent to the Fermi-Eyges transport equation up to terms of order δ. Expanding the density, $F(z,x-(\Theta+\alpha\phi)\delta,\Theta+\phi)$, in [3-5] to second order in a Taylor Series yields,

$$F(z,x-(\Theta+\alpha\phi)\delta,\Theta+\phi) \approx F(z,x,\Theta) - (\Theta+\alpha\phi)\delta \frac{dF}{dx} + \phi \frac{dF}{d\Theta} + \frac{(\Theta+\alpha\phi)^2\delta^2}{2} \cdot \frac{d^2F}{dx^2} + \phi^2 \frac{d^2F}{d\Theta^2} - \phi(\Theta+\alpha\phi) \frac{d^2F}{d\Theta dx} \qquad [3A-1]$$

Substituting back into the integral [3-5] and using the properties of the angular transition density,

$$\int_{-\infty}^{\infty} p(\Theta;\Theta+\phi)\, d\phi = 1 \qquad [3A-2a]$$

$$\int_{-\infty}^{\infty} \phi p(\Theta;\Theta+\phi)\, d\phi = 0 \qquad [3A-2b]$$

$$\int_{-\infty}^{\infty} \phi^2 p(\Theta;\Theta+\phi)\, d\phi = \frac{k\delta}{2} \qquad [3A-2c]$$

yields the equation,

$$F(z+\delta,x,\Theta) = F(z,x,\Theta) - \Theta\delta \frac{dF}{dx} + \frac{k\delta}{4} \cdot \frac{d^2F}{d\Theta^2} \qquad [3A-3]$$

To obtain this last expression, terms of order δ^2 or higher have been neglected. Notice that the factor, α, no longer appears, indicating that the choice of α is irrelevant.

An expansion of $F(z+\delta,x,\Theta)$ to first order for small δ gives,

$$F(z+\delta,x,\Theta) \approx F(z,x,\Theta) + \delta \frac{dF}{dz} \qquad [3A-4]$$

Finally, substitution of [3A-4] into [3A-3] yields the Fermi-Eyges transport equation,

$$\frac{dF}{dz} = -\Theta \frac{dF}{dx} + \frac{k}{4} \cdot \frac{d^2F}{d\Theta^2} \qquad [3A-5]$$

Appendix 3B

In this appendix, it is shown that the integral [3-6] is equivalent to the differential transport equation [3-7] up to terms of order δ. Expanding the density, $F(z,x-\tan(\Theta+\alpha\phi)\delta,\Theta+\phi)$, in [3-6] to second order in a Taylor Series yields,

$$F(z,x-\tan(\Theta+\alpha\phi)\delta,\Theta+\phi) \approx F(z,x,\Theta) - \tan(\Theta+\alpha\phi)\delta \frac{dF}{dx} + \phi \frac{dF}{d\Theta} + \frac{\tan^2(\Theta+\alpha\phi)\delta^2}{2}\bullet\frac{d^2F}{dx^2} + \frac{\phi^2}{2}\bullet\frac{d^2F}{d\Theta^2} - \phi\tan(\Theta+\alpha\phi)\delta \frac{d^2F}{dxd\Theta} \qquad [3B-1]$$

The function, $\tan(\Theta+\alpha\phi)$, may also be expanded in a Taylor Series to give,

$$\tan(\Theta+\alpha\phi) \approx \tan\Theta + \alpha\phi\bullet\sec^2\Theta + \alpha^2\phi^2\bullet\tan\Theta\bullet\sec^2\Theta \qquad [3B-2]$$

Substituting [3B-1] and [3B-2] into the integral [3-6], using the properties of the angular transition density [3A-2] and neglecting all terms of order δ^2 or higher we get,

$$F(z+\delta,x,\Theta) = F(z,x,\Theta) - \tan(\Theta)\delta \frac{dF}{dx} + \frac{k\delta}{4}\bullet\frac{d^2F}{d\Theta^2} \qquad [3B-3]$$

Finally, expanding the left hand side to first order in a Taylor Series for small increments, δ, gives the transport equation,

$$\frac{dF}{dz} = -\tan\Theta \frac{dF}{dx} + \frac{k}{4}\bullet\frac{d^2F}{d\Theta^2} \qquad [3B-4]$$

As expected, we have recovered the transport equation [3-7].

Chapter 4

Summary and Future Work

4.1 The Restricted Scattering Model

It was noted in the first chapter that one impediment to the use of electron beams in radiotherapy is the lack of a method of accurate dose prediction. The difficulty is partly due to the inadequacy of the Fermi-Eyges model for the description of electron transport deep in the scattering medium. The Fermi-Eyges model predicts that the mean square angle of travel increases monotonically with depth in the scattering medium and approaches infinity at a depth corresponding to the electron range. The restricted scattering model goes some way toward compensating for the weaknesses of the Fermi-Eyges model by forcing the angular spread of electrons to reach an equilibrium value in accordance with measured data (Roos et al.,1973).

The saturation in mean square angle of travel is achieved by modeling the variation of the angle of travel with depth as an Ornstein-Uhlenbeck stochastic process (Hoel et al.,1984). In this approach, a scattering bias is introduced such that electrons tend to scatter toward smaller angles rather than larger angles. The parameters specifying the jointly Gaussian angular-lateral probability density predicted by the restricted scattering model are given explicitly in section 2.2.

The improved prediction of the mean square angle of travel is indicated in figures 2.1, 2.2, 2.3 and 2.4. An improved prediction of the mean square lateral position is also demonstrated in chapter 2 in figures 2.5, 2.6 and 2.7. This leads to a more accurate representation of the broad beam dose profile in a homogeneous medium as indicated in figures 2.8, 2.9 and 2.10.

It should be noted that the restricted scattering model is not a physically based model in the sense that the angular restriction is not introduced to model a known physical interaction process. Rather, the angular restriction is introduced to model the observed macroscopic behaviour of a beam of electrons as it penetrates a dense scattering medium.

The testing of the restricted scattering model in a heterogeneous medium requires that the model be incorporated in a treatment planning algorithm. Since the restricted scattering model has the advantage of retaining the Gaussian features of the Fermi-Eyges model, it may be readily used in existing pencil beam algorithms. However, it is also possible to incorporate the restricted scattering model in the algorithm presented in chapter 3 by using the appropriate angular transition density. Both these possibilities remain for future work.

4.2 The Numerical Algorithm

In chapter 3, an integral equation is derived which allows the determination of the electron probability density at a depth, $z+\delta$, in the scattering medium given the probability density at a depth, z. This integral equation is shown to be consistent with the Fermi-Eyges model in the limit of small δ. A modification of the integral equation is then made where changes in lateral position are given by $\delta\bullet\tan\Theta$ rather than the small angle approximation, $\delta\bullet\Theta$. Both these integral equations are discretized for use in a computer algorithm.

Figures 3.5 and 3.6 show that the small angle equation is successful in reproducing the mean square angle of travel and mean square lateral position analytically predicted by the Fermi-Eyges model. Also, the small-angle-algorithm recovers analytically predicted pencil beam and broad beam profiles as indicated in figures 3.7 to 3.12. The discrepancy between the algorithm-generated results and the analytically predicted curves is generally within the discrete lateral increment size, $\blacktriangle x$. In section 3.7, it is shown that the large-angle-algorithm qualitatively reproduces the large angle scattering tails seen in Monte Carlo generated data (Lax et al.,1983).

In order to test the accuracy of the algorithm in inhomogeneous media, it is necessary to compare the algorithm results with measured data. However, in a heterogeneous medium, it is not possible to assume that the probability density calculated by the algorithm is proportional to dose (as was the case in a homogeneous medium). Therefore, the probability density which is generated by the algorithm must be converted to dose in order to make meaningful comparisons to measured data. A means of performing this conversion for the moments method (Storchi and Huizenga,1985) based on the input of measured broad beam depth dose data has been presented (Storchi and Huizenga,1986). Future implementations of the numerical method presented in chapter 3 may incorporate a similar empirical dose calculation scheme.

A more accurate "energy accounting" may be implemented in the numerical algorithm to improve its accuracy. Presently, the energy of electrons at a given lateral position is calculated using the energy of the electrons at the same lateral position in the plane above (see equation [3-10]). This approach does not account for the skewness of the electrons' paths. Electrons with oblique angles of travel follow relatively long paths in traversing a depth increment, δ. However, these electrons are assigned the same energy as electrons with shallow angles of travel which follow shorter paths over an increment of depth, δ. By defining several energy "bins" at each lateral position, a distribution of electron energies at each point may be calculated. The limited computer memory of the DEC LSI

11/73 computer does not allow this approach to be taken in the present work. However, the method of energy "binning" is a possibility for a future implementation of the numerical algorithm.

The work of chapter 3 indicates the feasibility of the use of the numerical algorithm in radiotherapy dose calculations. Also, using the large angle transport equation, it may be possible to improve upon the predictions of the Fermi-Eyges model.

References

Almond PR, Wright AE and Boone MLM (1967) "High energy electron dose perturbations in regions of tissue heterogeneity. Part II: Physical models of tissue heterogeneities." Radiology **88**: 1146-1153

Arfken G (1970) Mathematical Methods for Physicists Academic Press, New York (2nd ed)

Bagne F (1976) "Electron beam treatment planning system." Med. Phys. **3**:31-38

Bethe HA, Rose ME and Smith LP (1938) "The multiple scattering of electrons." Proc. Am. Philo. Soc. **78**: 573-585

Boone MLM, Jardine JH, Wright AE and Tapley NV (1967) "High energy electron dose perturbations in regions of tissue heterogeneity. Part I: In vivo dosimetry." Radiology **88**: 1136-1145

Brahme A (1985) "Current algorithms for computed electron beam dose planning." Radiotherapy and Oncology **3**: 347-362

Brahme A, Lax I and Andreo P (1981) "Electron beam dose planning using discrete Gaussian beams: Mathematical background." Acta Radiol. Oncol. **20**: 147-158

Bruinvis IAD, Van Amstel A, Elevelt AJ and Van der Laarse R (1983) "Calculation of electron beam dose distributions for arbitrarily shaped fields." Phys. Med. Biol. **28**: 667-683

Cygler J, Battista JJ, Scrimger JW, Mah E and Antolak J (1987) "Electron dose distributions in experimental phantoms: a comparison with 2D pencil beam calculations." Phys. Med. Biol. **32**: 1073-1086

Edwards FH and Coffey CW (1979) "A cumulative normal distribution model for simulation of electron beam profiles." Int. J. Radiat. Oncol. Biol. Phys. **5**: 127-133

Eyges L (1948) "Multiple scattering with energy loss." Phys. Rev. **74**: 1534-1535

Hoel P, Port S and Stone C (1984) Introduction to Stochastic Processes, Houghton Mifflin Company, Boston

Hogstrom KR, Mills MD and Almond PR (1981) "Electron beam dose calculations." Phys. Med. Biol. **26**: 445-459

Huizenga H and Storchi PRM (1985) "The use of computed tomography numbers in dose calculations for radiation therapy." Acta Radiol. Oncol. **24**: 509-519

Huizenga H and Storchi PRM (1987) "The in-air scattering of clinical electron beams as produced by accelerators with scanning beams and diaphragm collimators." Phys. Med. Biol. **32**: 355-363

ICRU (1984) "Stopping powers for electrons and positrons." International Commission on Radiation Units and Measurements, Report 37

ICRU (1984b) "Radiation dosimetry: Electron beams with energies between 1 and 50 MeV." International Commission on Radiation Units and Measurements, Report 35

Jette D, Pagnamenta A, Lanzl LH and Rozenfeld M (1983) "The application of multiple scattering theory to therapeutic electron dosimetry." Med. Phys. **10**: 141-146

Jette D (1988) "Electron dose calculation using multiple-scattering theory: A Gaussian multiple scattering theory." Med. Phys. **15**: 123-137

Karlin S and Taylor HM (1975) A First Course in Stochastic Processes Second edition, Academic Press, New York

Kawachi K (1975) "Calculation of electron dose distribution for radiotherapy treatment planning." Phys. Med. Biol. **20**: 571-577

Laughlin JS (1965) "High energy electron treatment planning for inhomogeneities." Brit. J. Radiol. **38**: 143-147

Lax I, Brahme A and Andreo P (1983) "Electron beam dose planning using Gaussian beams: Improved radial dose profiles." Acta Radiol. **Suppl. 364**: 49-59

Lillicrap SC, Wilson P and Boag JW (1975) "Dose distributions in high energy electron beams: Production of broad beam distributions from narrow beam data." Phys. Med. Biol. **20**: 30-38

Loevinger R, Karzmark CJ and Weissbluth M (1961) "Radiation therapy with high energy electrons: Part I. Physical considerations, 10 to 60 MeV." Radiology **77**: 906-927

Mah E, Antolak J, Scrimger JW and Battista JJ (1989) "Experimental evaluation of a 2D and 3D electron pencil beam algorithm." Phys. Med. Biol. **34**: 1179-1194

McParland BJ (1989) "A derivation of the electron mass scattering power for electron dose calculations." Nuc. Instr. Meth. Phys. Res. **A274**: 592-596

Perry and Holt (1980) "A model for calculating the effects of small inhomogeneities on electron beam dose distributions." Med. Phys. **7**: 207-215

Roos H, Drepper P and Harder D (1973) "The transition from multiple scattering to complete diffusion of high-energy electrons." in Proceedings of the Fourth Symposium on Microdosimetry, Euratom EUR 5122 d-e-f (eds J.Booz, R.Eichel, A.Waker and H.G.Ebert) pp 779-798

Rossi B (1952) High Energy Particles, Prentice-Hall Inc, New Jersey, pp 69-71

Rossi B and Greissen K (1941) "Cosmic ray theory." Rev. Mod. Phys. **13**: 240-309

Sandison GA and Huda W (1988) "Application of Fermi scattering theory to a magnetically scanned electron linear accelerator." Med. Phys. **15**: 498-510

Sandison GA, Huda W, Battista JJ and Savoie D (1989) "Comparison of methods to determine electron pencil beam spread in tissue-equivalent media." Med. Phys. **16**: 881-888

Shiu AS and Hogstrom KR (1987) "A pencil-beam redefinition algorithm for electron dose distributions." in The Use of Computers in Radiation Therapy, editors IAD Bruinvis et al., Elsevier Science Publishers, North-Holland, pp 69-72

Shortt KR, Ross CK, Bielajew AF and Rogers DWO (1986) "Electron beam dose distributions near standard inhomogeneities." Phys. Med. Biol. **1**: 235-249

Storchi PRM and Huizenga H (1985) "On a numerical approach of the pencil beam model." Phys. Med. Biol. **30**: 467-473

Storchi PRM and Huizenga H (1986) "Progress on the moments method for clinical electron beam planning." presented at the 28th Annual Meeting of the American Association of Physicists in Medicine, Lexington, Kentucky

Storchi PRM, Van der Linden R and Huizenga H (1987) "Mathematical generalization of the moment method for clinical electron beam dose calculation." in The Use of Computers in Radiation Therapy, editors IAD Bruinvis et al., Elsevier Science Publishers, North-Holland, pp 145-147

Werner BL, Khan FM and Deibel FC (1982) "A model for calculating electron beam scattering in treatment planning." Med. Phys. **9**: 180-187

White D (1978) "Tissue substitutes in experimental radiation physics." Med. Phys. **5**: 467-479

Zerby CD and Keller FL (1967) "Electron transport theory, calculations, and experiments." Nucl. Sci. Eng. **27**: 190-218